Available online at www.sciencedirect.com
ScienceDirect
Journal of Sound and Vibration 319 (2009) 1036–1066
JOURNAL OF SOUND AND VIBRATION
www.elsevier.com/locate/jsvi

Ground-borne vibration due to static and dynamic axle loads of InterCity and high-speed trains

G. Lombaert*, G. Degrande

Department of Civil Engineering, K.U. Leuven, Kasteelpark Arenberg 40, B-3001 Leuven, Belgium

Received 14 November 2007; received in revised form 2 July 2008; accepted 8 July 2008
Handling Editor: C.L. Morfey
Available online 19 August 2008

Abstract

In predictions of railway-induced vibrations, a distinction is generally made between the quasi-static and dynamic excitation. The quasi-static excitation is related to the static component of the axle loads. The dynamic excitation is due to dynamic train–track interaction, which is generated by a large number of excitation mechanisms, such as the spatial variation of the support stiffness and the wheel and track unevenness. In the present paper, the quasi-static excitation and the dynamic excitation due to random track unevenness are evaluated by means of numerical predictions. A solution strategy is presented that allows for the evaluation of the second-order statistics of the response due to dynamic excitation based on the power spectral density function of the track unevenness. Due to the motion of the train, the second-order statistics of the response at a fixed point in the free field are non-stationary and an appropriate solution procedure is required. The quasi-static and dynamic contribution to the track and free-field response are analysed for the case of InterCity and high-speed trains running at a subcritical train speed. It is shown how the train speed affects the quasi-static and dynamic contribution. Finally, results of numerical predictions for different train speeds are compared with field measurements that have been performed at a site along the high-speed line L2 Brussels–Köln within the frame of homologation tests.

1. Introduction

The development of numerical models for railway-induced vibrations has received considerable attention in the past 10 years. The increased interest is partly due to the development of the high-speed train (HST) network in Europe, the USA and Asia.

In these models, a distinction is generally made between the quasi-static and dynamic excitation. The quasi-static excitation is related to the static component of the axle loads. Due to the motion of the train, the quasi-static response is time dependent. For HST tracks on soft soils, the train speed can be close to or even larger than the critical phase velocity of the coupled track–soil system, in which case the quasi-static excitation leads to high vibrations and track displacements, affecting track stability and safety [1,2]. The dynamic excitation is

---

*Corresponding author. Tel.: +32 16 32 17 72; fax: +32 16 32 19 88.
E-mail address: geert.lombaert@bwk.kuleuven.be (G. Lombaert).

0022-460X/$ - see front matter
doi:10.1016/j.jsv.2008.07.003

determined by dynamic train–track interaction due to several excitation mechanisms, such as the spatial variation of the support stiffness and the wheel and track unevenness [3–5]. Track unevenness is usually assumed to be a stationary random process and characterized by its power spectral density (PSD) function [6].

In numerical models, the geometry of the track and the soil is often assumed to be invariant in the longitudinal direction of the track. This allows the use of efficient "two-and-a-half dimensional" solution procedures, based on a Fourier transform with respect to the coordinate along the track. Alternative methods based on the finite element method require appropriate procedures [7] to account for the unbounded domain and to avoid spurious reflections at boundaries. Aubry et al. [8] have applied a two-and-a-half-dimensional procedure to study the response of an infinitely long beam, coupled to an elastic half-space, due to a moving load. The methodology has been applied by Sheng et al. [9,10] to an infinite layered beam model for the track, coupled to a layered half-space. More recently, this model has been elaborated to account for dynamic train–track interaction [11,12]. Metrikine et al. [2] study the stability of a moving train bogie, modelled as a two-degree-of-freedom system. This vehicle model is coupled to a beam of infinite length for the track and a homogeneous half-space model for the soil, based on developments by Metrikine and Popp [13] and Dieterman and Metrikine [14]. Lombaert et al. [15,16] apply this methodology in a boundary element formulation to predict vibrations induced by road [15] and railway traffic [16]. The model has been validated by means of field measurements [16] and used to assess the vibration isolation efficiency of a floating slab track [17].

Similar models have also been developed for the prediction of vibrations due to subway traffic. Forrest and Hunt [18,19] and Hussein and Hunt [20] present the "pipe-in-pipe" model where a shell model is used for the tunnel, while the soil is represented by an elastic full space with a cylindrical cavity. Recently, the soil model has been elaborated to account for the free surface of an elastic half-space, as well as for horizontal layering [21].

Coupled two-and-a-half-dimensional finite element and boundary element formulations for railway traffic at grade and in tunnels have been presented by Sheng et al. [22] and Andersen and Jones [23], respectively. Whereas the geometry is still longitudinally invariant, an arbitrary cross-section of the track can be considered. For subway tunnels with a periodic geometry, a similar methodology is proposed by Clouteau et al. [24] and Degrande et al. [25], where a Flocquet transform is used instead of a Fourier transform. The advantage is that only a discretisation of a single reference cell is needed to solve the dynamic track–tunnel–soil interaction problem. The response of periodic structures subjected to moving loads is discussed by Chebli et al. [26]. These developments have been recently applied by Gupta et al. [27] to predict vibrations due to subway traffic in Beijing.

In the present paper, the quasi-static excitation and the dynamic excitation due to random track unevenness are evaluated. The quasi-static and dynamic contribution to the track and free-field response are analysed for both InterCity and HSTs. The case is considered where the train speed is below the critical phase velocity of the coupled track–soil system. A comparison is made with field measurements that have been performed during the homologation tests of the high-speed line L2 between Brussels and Köln. During these tests, vibrations of the track and in the free field have been measured for several passages of the Thalys HST and an InterCity train. These data are complementary to earlier data from homologation tests on the line L1 between Brussels and Paris [28] that have been used by Degrande and Lombaert [29], Paolucci and Spinelli [30] and Galvín and Domínguez [31] to validate numerical prediction models.

The outline of this paper is as follows. First, the numerical prediction of railway-induced vibrations is briefly recapitulated. It is shown how the response due to multiple moving loads is calculated from the transfer function between the track and the free field. The reader is referred to aforementioned publications on two-and-a-half-dimensional models for more details on the calculation of this transfer function. Quasi-static and dynamic axle loads are distinguished. The dynamic axle loads are due to random rail unevenness, characterized by its PSD function. A solution strategy is presented for the calculation of the non-stationary second-order statistical characteristics of the response based on the PSD of the random track unevenness. This allows for the computation of the mean square response in both the time and the frequency domain at a moderate computational cost. Second, an analysis is made of the influence of the train speed and the type of train on the quasi-static and dynamic excitation. It is shown how different samples of track unevenness from a given PSD function yield different results. Third, measured and predicted one-third octave band spectra and running rms values of the track and free-field velocity are analysed.

2. The prediction of vibrations due to moving loads

2.1. Dynamic loads travelling on longitudinally invariant media

The response of the coupled track–soil system due to multiple moving loads is calculated from the 3×3 transfer matrix $\mathbf{H}(\mathbf{x}', \mathbf{x}, t)$. Each element $h_{ij}(\mathbf{x}', \mathbf{x}, t)$ of this matrix represents the response at a point $\mathbf{x}$ in the direction $\mathbf{e}_j$ at a time t due to an impulse load at a point $\mathbf{x}'$ in the direction $\mathbf{e}_i$ at the time $t = 0$. The response $\mathbf{u}(\mathbf{x}', t)$ due to an arbitary body load $\rho\mathbf{b}(\mathbf{x}, t)$ is calculated by means of the dynamic reciprocity theorem:

$$\mathbf{u}(\mathbf{x}', t) = \int_{-\infty}^{t} \int_{\Omega} \mathbf{H}(\mathbf{x}', \mathbf{x}, t - \tau)\rho\mathbf{b}(\mathbf{x}, \tau)\, \mathrm{d}\mathbf{x}\, \mathrm{d}\tau \tag{1}$$

where Ω is the domain of the coupled track–soil system. In the following, dynamic reciprocity is used to replace $\mathbf{H}(\mathbf{x}', \mathbf{x}, t - \tau)$ by $\mathbf{H}^{\mathrm{T}}(\mathbf{x}, \mathbf{x}', t - \tau)$. For n_a loads moving at a constant speed v in the direction $\mathbf{e}_y$, the body load $\rho\mathbf{b}(\mathbf{x}, t)$ is equal to

$$\rho\mathbf{b}(\mathbf{x}, t) = \sum_{k=1}^{n_a} \delta(\mathbf{x} - \mathbf{x}_k(t))\mathbf{g}_k(t) \tag{2}$$

where $\mathbf{x}_k(t) = \mathbf{x}_{k0} + vt\mathbf{e}_y$ is the time-dependent position of the k-th load, $\mathbf{x}_{k0}$ is the position at the time $t = 0$ and $\mathbf{g}_k(t)$ is the time history of the k-th axle load. Axle loads are assumed to be positive when their action on the track is in the positive coordinate direction (Fig. 1).

The response due to the moving loads is calculated as follows:

$$\mathbf{u}(\mathbf{x}', t) = \sum_{k=1}^{n_a} \int_{-\infty}^{t} \mathbf{H}^{\mathrm{T}}(\mathbf{x}_k(\tau), \mathbf{x}', t - \tau)\mathbf{g}_k(\tau)\, \mathrm{d}\tau \tag{3}$$

In the particular case where Ω is invariant with respect to the longitudinal direction $\mathbf{e}_y$ (Fig. 1), the transfer function is unaffected by an arbitrary translation $l\mathbf{e}_y$ of the source and the receiver position. If l equals $-(y_{k0} + v\tau)$, the source position $\mathbf{x}_k(\tau) - l\mathbf{e}_y = \{x_{k0}, 0, z_{k0}\}^{\mathrm{T}}$ no longer depends on the time τ and can be omitted in the argument of the transfer function. Furthermore, the coordinates x' and z' of the receiver position $\mathbf{x}' = \{x', y', z'\}^{\mathrm{T}}$ are assumed to be fixed, so that Eq. (3) is rewritten as follows:

$$\mathbf{u}(y', t) = \sum_{k=1}^{n_a} \int_{-\infty}^{t} \mathbf{H}^{\mathrm{T}}(y' - y_{k0} - v\tau, t - \tau)\mathbf{g}_k(\tau)\, \mathrm{d}\tau \tag{4}$$

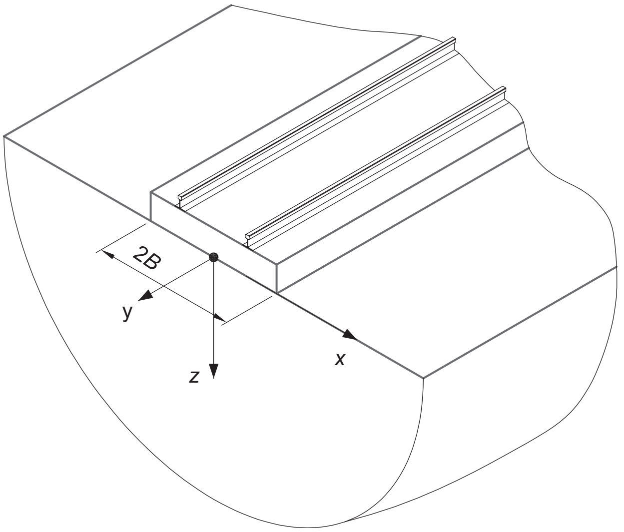

Fig. 1. Problem geometry.

In the following, the prime on the receiver coordinate y is omitted. A double forward Fourier transform from the space–time domain (y, t) leads to the following expression in the wavenumber–frequency domain (k_y, ω):

$$\tilde{\mathbf{u}}(k_y, \omega) = \sum_{k=1}^{n_a} \tilde{\mathbf{H}}^{\mathrm{T}}(k_y, \omega)\hat{\mathbf{g}}_k(\omega - k_y v)\exp(+\mathrm{i}k_y y_{k0}) \tag{5}$$

where a tilde denotes the representation in the frequency–wavenumber domain and a hat the representation in the frequency domain. Müller and Huber [32] were among the first to propose such a formulation to compute the response of a layered elastic half-space due to a moving load. An inverse wavenumber transform gives the frequency content of the response:

$$\hat{\mathbf{u}}(y, \omega) = \sum_{k=1}^{n_a} \frac{1}{2\pi}\int_{-\infty}^{+\infty} \tilde{\mathbf{H}}^{\mathrm{T}}(k_y, \omega)\hat{\mathbf{g}}_k(\omega - k_y v)\exp[-\mathrm{i}k_y(y - y_{k0})]\,\mathrm{d}k_y \tag{6}$$

This expression is particularly useful when the transfer function is available in the frequency–wavenumber domain. An efficient evaluation of the inverse wavenumber transform is proposed by Lieb [33] and Grundmann et al. [34] based on an additional wavelet transform of the response in the frequency–wavenumber domain.

A change of variables $\tilde{\omega} = \omega - k_y v$ gives the following expression:

$$\hat{\mathbf{u}}(y, \omega) = \sum_{k=1}^{n_a} \frac{1}{2\pi v}\int_{-\infty}^{+\infty} \tilde{\mathbf{H}}^{\mathrm{T}}\left(\frac{\omega - \tilde{\omega}}{v}, \omega\right)\hat{\mathbf{g}}_k(\tilde{\omega})\exp\left[-\mathrm{i}\left(\frac{\omega - \tilde{\omega}}{v}\right)(y - y_{k0})\right]\mathrm{d}\tilde{\omega} \tag{7}$$

The transfer function is evaluated at a wavenumber $k_y = (\omega - \tilde{\omega})/v$ that couples the frequency $\tilde{\omega}$ emitted by the moving source to the frequency ω observed at the receiver. Due to the Doppler effect, a source at a fixed frequency $\tilde{\omega}$ contributes to the response in a frequency range $[\tilde{\omega}/(1 + v/C), \tilde{\omega}/(1 - v/C)]$, determined by the smallest phase velocity C of interest. Ditzel et al. [35] have identified the Doppler effect in field measurements of railway-induced vibrations.

In the following, the response of the coupled track–soil system due to a train passage is calculated. A distinction is made between the quasi-static and dynamic contribution to the response, based on a decomposition of the time history $\mathbf{g}_k(t)$ of each axle load into a static component $\mathbf{g}_{sk}$ and a dynamic component $\mathbf{g}_{dk}(t)$.

The dynamic component $\mathbf{g}_{dk}(t)$ of the axle loads is calculated by means of a compliance formulation in a moving frame of reference [36]. This requires the calculation of the track response in a coordinate system $\hat{\mathbf{x}} = \{x, \hat{y}, z\}^{\mathrm{T}}$ with $\hat{y} = y - vt$. The latter is derived from Eq. (6) by an additional inverse Fourier transform with respect to ω and by replacing y by $\hat{y} + vt$ on the right-hand side:

$$\mathbf{u}(\hat{y}, t) = \sum_{k=1}^{n_a} \frac{1}{2\pi}\int_{-\infty}^{+\infty} \frac{1}{2\pi}\int_{-\infty}^{+\infty} \tilde{\mathbf{H}}^{\mathrm{T}}(k_y, \omega)\hat{\mathbf{g}}_{dk}(\omega - k_y v)\exp[-\mathrm{i}k_y(\hat{y} + vt - y_{k0})]\,\mathrm{d}k_y\exp(\mathrm{i}\omega t)\,\mathrm{d}\omega \tag{8}$$

A change of variables $\omega = \tilde{\omega} + k_y v$ leads to the following expression:

$$\mathbf{u}(\hat{y}, t) = \frac{1}{2\pi}\int_{-\infty}^{+\infty} \sum_{k=1}^{n_a}\left[\frac{1}{2\pi}\int_{-\infty}^{+\infty} \tilde{\mathbf{H}}^{\mathrm{T}}(k_y, \tilde{\omega} + k_y v)\exp[-\mathrm{i}k_y(\hat{y} - y_{k0})]\,\mathrm{d}k_y\right]\hat{\mathbf{g}}_{dk}(\tilde{\omega})\exp(\mathrm{i}\tilde{\omega}t)\,\mathrm{d}\tilde{\omega} \tag{9}$$

For each axle k, the response is obtained as the inverse Fourier transform with respect to $\tilde{\omega}$ of the product of the bracketed term and the frequency content $\hat{\mathbf{g}}_{dk}(\tilde{\omega})$ of the moving load. Each column of the bracketed term represents the response in a moving frame of reference due to an impulsive moving load located at y_{k0} at the time $t = 0$.

2.2. *Response due to quasi-static excitation*

The static component $\mathbf{g}_{sk}$ of the axle loads is equal to $w_k\mathbf{e}_z$, where w_k is the weight carried by axle k. Introducing the Fourier transform $\hat{\mathbf{g}}_{sk} = w_k\mathbf{e}_z 2\pi\delta(\omega)$ in Eq. (7) gives the quasi-static response:

$$\hat{\mathbf{u}}(y, \omega) = \left[\frac{1}{v}\tilde{\mathbf{H}}^{\mathrm{T}}\left(\frac{\omega}{v}, \omega\right)\mathbf{e}_z\exp\left(-\mathrm{i}\frac{\omega}{v}y\right)\right]\left[\sum_{k=1}^{n_a} w_k\exp\left(\mathrm{i}\frac{\omega}{v}y_{k0}\right)\right] \tag{10}$$

The first bracketed term on the right-hand side is the response due to a unit axle load, while the second bracketed term represents a modulation of the response, determined by the distribution of the weight over the axles and by the train speed v [29,37,38]. This expression is rewritten as follows:

$$\hat{\mathbf{u}}(y,\omega) = \left[\frac{w_l}{v}\tilde{\mathbf{H}}^{\mathrm{T}}\left(\frac{\omega}{v},\omega\right)\mathbf{e}_z \exp\left(-\mathrm{i}\frac{\omega}{v}(y-y_{l0})\right)\right]\left[\sum_{k=1}^{n_a}\frac{w_k}{w_l}\exp\left(\mathrm{i}\frac{\omega}{v}(y_{k0}-y_{l0})\right)\right] \tag{11}$$

where the first bracketed term on the right-hand side now represents the response due to an (arbitrary) axle l. In the following, the quasi-static response due to a single axle is calculated according to Eq. (11) and compared with the dynamic response due to a single axle.

2.3. The dynamic axle loads

The calculation of the dynamic component $\mathbf{g}_{dk}(t)$ of the axle loads is based on the assumption of a perfect contact between the train and the track. For each axle k, this requires the continuity of displacements at the contact point between the axle and the track:

$$\mathbf{u}_{ak}(t) = \mathbf{u}_{tk}(t) + \mathbf{u}_{w/rk}(t) \tag{12}$$

where $\mathbf{u}_{ak}(t)$ is the displacement of axle k and $\mathbf{u}_{tk}(t)$ is the track displacement at the k-th axle position $\hat{\mathbf{x}}_k$ in the moving frame of reference. The vector $\mathbf{u}_{w/rk}(t)$ is the combined wheel/rail unevenness perceived by axle k. In the present approach, an irregular wheel or track geometry is only accounted for in the term $\mathbf{u}_{w/rk}(t)$ that represents the wheel/rail unevenness, while its effect on the dynamic behaviour of the wheel or the track is disregarded. The axle and track displacements in Eq. (12) are calculated for perfectly smooth wheels and a longitudinally invariant track, respectively.

When only vertical track unevenness $u_{rz}(y)$ is accounted for, $\mathbf{u}_{w/rk}(t)$ becomes:

$$\mathbf{u}_{w/rk}(t) = u_{rz}(y_{k0} + vt)\mathbf{e}_z \tag{13}$$

and all axles experience the same excitation, apart from a time delay. Eq. (12) is now written in terms of the dynamic loads $\mathbf{g}_{dk}(t)$. First, Eq. (9) is used to calculate the track displacement $\hat{\mathbf{u}}_{tk}(\omega)$:

$$\hat{\mathbf{u}}_{tk}(\omega) = \sum_{l=1}^{n_a}\left[\frac{1}{2\pi}\int_{-\infty}^{+\infty}\tilde{\mathbf{H}}^{\mathrm{T}}(k_y,\omega+k_y v)\exp[-\mathrm{i}k_y(y_{k0}-y_{l0})]\,\mathrm{d}k_y\right]\hat{\mathbf{g}}_{dl}(\omega) \tag{14}$$

The bracketed term is the 3×3 matrix $\hat{\mathbf{C}}^t_{kl}(\omega)$ that relates the track displacement at axle k to the dynamic load at axle l. These matrices are collected into the $3n_a \times 3n_a$ track compliance matrix $\hat{\mathbf{C}}^t(\omega)$ that links the vector $\hat{\mathbf{u}}_t(\omega)$ with the track displacements at all axles to the vector $\hat{\mathbf{g}}_d(\omega)$ with dynamic loads:

$$\hat{\mathbf{u}}_t(\omega) = \hat{\mathbf{C}}^t(\omega)\hat{\mathbf{g}}_d(\omega) \tag{15}$$

A mechanical model of the train is used to calculate the vehicle compliance matrix $\hat{\mathbf{C}}^v(\omega)$:

$$\hat{\mathbf{u}}_a(\omega) = -\hat{\mathbf{C}}^v(\omega)\hat{\mathbf{g}}_d(\omega) \tag{16}$$

The signs in Eqs. (15) and (16) are different due to the convention that axle loads are positive when their action on the track is in the positive coordinate direction. Introducing Eqs. (15) and (16) in Eq. (12) leads to the following system of equations for the dynamic loads $\hat{\mathbf{g}}_d(\omega)$:

$$[\hat{\mathbf{C}}^t(\omega) + \hat{\mathbf{C}}^v(\omega)]\hat{\mathbf{g}}_d(\omega) = -\hat{\mathbf{u}}_{w/r}(\omega) \tag{17}$$

where $\hat{\mathbf{u}}_{w/r}(\omega)$ collects the unevenness $\hat{\mathbf{u}}_{w/rk}(\omega)$ at all axles. The inverse $[\hat{\mathbf{C}}^t(\omega) + \hat{\mathbf{C}}^v(\omega)]^{-1}$ of the combined track and vehicle compliance can be considered as the dynamic stiffness of the coupled vehicle–track system.

Similar expressions as Eq. (17) are given by Sheng et al. [12] and Auersch [37], who couples a finite element model for a finite part of the track to a boundary element model for the soil. Grundmann and Lenz [39] present an alternative solution that allows for the coupling of a nonlinear single-degree-of-freedom system to the track.

When vertical rail unevenness dominates, the term on the right-hand side of Eq. (17) can be further elaborated as

$$\hat{\mathbf{u}}_{w/r}(\omega) = \hat{\mathbf{T}}(\omega)\frac{1}{v}\tilde{u}_{rz}\left(-\frac{\omega}{v}\right) \tag{18}$$

where $\tilde{u}_{rz}(k_y)$ is the wavenumber transform of the rail unevenness $u_{rz}(y)$ and $\hat{\mathbf{T}}(\omega)$ is a $3n_a \times 1$ vector that collects the phase shift for each axle:

$$\hat{\mathbf{T}}(\omega) = \left\{\ldots, 0, \exp\left(\frac{\mathrm{i}\omega y_{k0}}{v}\right), 0, \ldots\right\}^{\mathrm{T}} \tag{19}$$

In this paper, random track unevenness $u_{rz}(y)$ is modelled as a stationary Gaussian random process characterized by its one-sided PSD function $\tilde{S}_{rzz}(k_y)$ [m^2/(rad/m)] [6]. The spectral representation theorem [40,41] is used to generate samples $u_{rz}(y)$ of track unevenness as a superposition of harmonic functions with random phase angles:

$$u_{rz}(y) = \sum_{m=1}^{n} \sqrt{2\tilde{S}_{rzz}(k_{ym})\Delta k_y}\cos(k_{ym}y - \theta_m) \tag{20}$$

where $k_{ym} = m\Delta k_y$ is the wavenumber sampling, Δk_y the wavenumber bin and θ_m are independent random phase angles uniformly distributed in the interval $[0, 2\pi]$. The samples have a period $Y = 2\pi/\Delta k_y$ and are asymptotically Gaussian as n tends to infinity and Δk_y tends to zero for a fixed value of $k_y^{\max} = n\Delta k_y$. The second term on the right-hand side of Eq. (18) becomes:

$$\frac{1}{v}\tilde{u}_{rz}\left(-\frac{\omega}{v}\right) = \sum_{m=1}^{n}\frac{-1}{\sqrt{v}}\sqrt{2\tilde{S}_{rzz}\left(\frac{|\omega_m|}{v}\right)\Delta\omega_m}[\pi\delta(\omega-\omega_m)\mathrm{e}^{+\mathrm{i}\theta_m} + \pi\delta(\omega+\omega_m)\mathrm{e}^{-\mathrm{i}\theta_m}] \tag{21}$$

where $\Delta\omega_m = v\Delta k_y$ and $\omega_m = -vk_{ym}$. For different samples of unevenness, the harmonic functions have the same modulus, but a different random phase. The influence of the train speed v on the modulus of the perceived unevenness can easily be quantified when the PSD $\tilde{S}_{rzz}(k_y)$ is proportional to k_y^{-n} in the relevant range of wavelengths. For trains running at speeds between 150 and 330 km/h and a frequency range between 1 and 150 Hz, this range of wavelengths is situated between 0.3 and 100 m. When the PSD $\tilde{S}_{rzz}(k_y)$ is proportional to k_y^{-n} with $n>1$, $\tilde{S}_{rzz}(|\omega_m|/v)$ increases with the speed v as v^n for a fixed sampling in the frequency domain. The modulus of the perceived unevenness in Eq. (21) therefore increases as $v^{0.5(n-1)}$. In many cases, however, the dependence on of the PSD on the wavenumber is more complex and the influence of the vehicle speed is less straightforward.

The system of equations (17) is now further elaborated by means of Eqs. (18), (19) and (21):

$$\hat{\mathbf{g}}_d(\omega) = -[\hat{\mathbf{C}}^t(\omega) + \hat{\mathbf{C}}^v(\omega)]^{-1}\hat{\mathbf{T}}(\omega)\sum_{m=1}^{n}\frac{-1}{\sqrt{v}}\sqrt{2\tilde{S}_{rzz}\left(\frac{|\omega_m|}{v}\right)\Delta\omega_m}[\pi\delta(\omega-\omega_m)\mathrm{e}^{+\mathrm{i}\theta_m} + \pi\delta(\omega+\omega_m)\mathrm{e}^{-\mathrm{i}\theta_m}] \tag{22}$$

An inverse Fourier transform of this equation shows that the time history of each axle load is a superposition of harmonic functions. For different realizations of the track unevenness according to Eq. (21), different values are obtained for the random phase angles θ_m, while the amplitude of the harmonic functions remains the same. When the PSD $\tilde{S}_{rzz}(k_y)$ is proportional to k_y^{-n} with $n>1$ and the track compliance matrix $\hat{\mathbf{C}}^t(\omega)$ is assumed to be unaffected by the train speed v, the modulus $|\hat{\mathbf{g}}_d(\omega)|$ of the dynamic loads increases as $v^{0.5(n-1)}$.

2.4. Response due to dynamic excitation

The dynamic axle loads $\hat{\mathbf{g}}_{dk}(\omega)$ are now introduced in Eq. (7):

$$\hat{\mathbf{u}}(y, \omega) = \sum_{k=1}^{n_a}\frac{1}{2\pi}\int_{-\infty}^{+\infty}\frac{1}{v}\tilde{\mathbf{H}}^{\mathrm{T}}\left(\frac{\omega-\tilde{\omega}}{v}, \omega\right)\exp\left[-\mathrm{i}\left(\frac{\omega-\tilde{\omega}}{v}\right)(y - y_{k0})\right]\hat{\mathbf{g}}_{dk}(\tilde{\omega})\,\mathrm{d}\tilde{\omega} \tag{23}$$

Due to the Doppler effect, the response at a fixed receiver frequency ω is determined by dynamic axle loads $\hat{\mathbf{g}}_{dk}(\tilde{\omega})$ with a source frequency $\tilde{\omega}$ in a frequency range $[\omega(1-v/C), \omega(1+v/C)]$. Even when the application of Eq. (22) results in a deterministic value for the modulus $|\hat{\mathbf{g}}_{dk}(\tilde{\omega})|$, the superposition of contributions for different source frequencies $\tilde{\omega}$ results in a random value for the modulus $|\hat{\mathbf{u}}(y,\omega)|$ of the response. The effect of the train speed on the modulus $|\hat{\mathbf{u}}(y,\omega)|$ cannot be predicted in a similar way as for the dynamic axle loads as each sample of track unevenness results in a different response. In the following subsection, a methodology is presented for the calculation of the ensemble average response in both the time and frequency domain.

To compare the ensemble average response to the response for a single sample, Eq. (23) is rewritten as follows:

$$\hat{\mathbf{u}}(y,\omega) = \sum_{k=1}^{n_a} \frac{1}{2\pi} \int_{-\infty}^{+\infty} \hat{\mathbf{U}}^{\mathrm{T}}(y - y_{k0}, \omega, \tilde{\omega}) \hat{\mathbf{g}}_{dk}(\tilde{\omega})\, \mathrm{d}\tilde{\omega} \tag{24}$$

where $\hat{\mathbf{U}}^{\mathrm{T}}(y - y_{k0}, \omega, \tilde{\omega})$ is the following 3×3 matrix:

$$\hat{\mathbf{U}}^{\mathrm{T}}(y - y_{k0}, \omega, \tilde{\omega}) = \frac{1}{v} \tilde{\mathbf{H}}^{\mathrm{T}}\left(\frac{\omega - \tilde{\omega}}{v}, \omega\right) \exp\left[-\mathrm{i}\left(\frac{\omega - \tilde{\omega}}{v}\right)(y - y_{k0})\right] \tag{25}$$

Comparing this expression to Eq. (7) shows that each element $\hat{u}_{ij}(y,\omega,\omega_m)$ is the response at a point $\{x,y,z\}^{\mathrm{T}}$ in the direction $\mathbf{e}_j$ due to a harmonic moving load $\mathbf{g}(t) = \mathbf{e}_i \exp(\mathrm{i}\tilde{\omega}t)$ at a position $\{x, y_{k0} + vt, z\}^{\mathrm{T}}$.

2.5. *Ensemble average response due to random track unevenness*

Track unevenness is often modelled as a stationary Gaussian random process characterized by its PSD function [6]. When Eq. (12) is applied and the axle and track displacements are calculated for perfectly smooth wheels and a longitudinally invariant track, respectively, the time history of the dynamic load at each axle is also a stationary random process. In this case, Eqs. (17) and (18) can be used to calculate the PSD of the dynamic axle loads from the PSD of the track unevenness according to classical random vibration theory [42]. In a similar way, the statistical characteristics of the response in a moving frame of reference can be calculated [19,43].

The response at a fixed point, however, is a non-stationary random process. In the case of road traffic, the vehicle speed is small with respect to the wave velocities in the ground, and the motion of the axle loads can be neglected to approximate the instantaneous power spectrum of ground vibrations by means of stationary stochastic methods [44]. These methods also apply when the response at a certain distance from the road due to a continuous stream of vehicles is considered [45]. Otherwise, a non-stationary auto-correlation function is needed to characterize the second-order statistics of the response at a fixed point $\mathbf{x}$:

$$\mathbf{R}_{\mathbf{u}}(y, t_1, t_2) = \langle \mathbf{u}(y, t_1) \otimes \mathbf{u}(y, t_2) \rangle \tag{26}$$

where $\otimes$ is the outer product and the angle brackets denote the average with respect to the random track unevenness. Lombaert et al. [46] calculate alternatively the Wigner–Ville distribution or the instantaneous power spectrum of the response. Recently, Lu et al. [47] have applied a more simple formulation to compute the mean square response, i.e. the case where $t_1 = t_2$. In the following, such a strategy is presented for the mean square response in the time and frequency domain.

The time history of the response in the right-hand side of Eq. (26) is calculated by means of Eq. (4):

$$\mathbf{R}_{\mathbf{u}}(y, t_1, t_2) = \sum_{k=1}^{n_a} \sum_{l=1}^{n_a} \left[\int_{-\infty}^{t_1} \mathbf{H}^{\mathrm{T}}(y - y_{k0} - v\tau, t_1 - \tau_1) \otimes \int_{-\infty}^{t_2} \mathbf{H}^{\mathrm{T}}(y - y_{l0} - v\tau, t_2 - \tau_2) \right] : \langle \mathbf{g}_k(\tau_1) \otimes \mathbf{g}_l(\tau_2) \rangle \, \mathrm{d}\tau_1 \, \mathrm{d}\tau_2 \tag{27}$$

The term between angle brackets is the averaged outer product of the time histories $\mathbf{g}_k(\tau_1)$ and $\mathbf{g}_l(\tau_2)$ of the dynamic loads at axles k and l. When the track unevenness is a stationary random process and the track geometry is longitudinally invariant, the time histories of the dynamic loads are stationary random processes as well. The averaged outer product $\langle \mathbf{g}_k(\tau_1) \otimes \mathbf{g}_l(\tau_2) \rangle$ is equal to the cross-correlation function $\mathbf{R}_{\mathbf{g}kl}(\tau_2 - \tau_1)$ of the dynamic load at two axles k and l and is written as the inverse Fourier transform of the (two-sided) 3×3

cross-PSD matrix $\hat{\mathbf{S}}_{\mathbf{g}kl}(\tilde{\omega})$ [N^2/(rad/s)]:

$$\langle \mathbf{g}_k(\tau_1) \otimes \mathbf{g}_l(\tau_2) \rangle = \int_{-\infty}^{+\infty} \hat{\mathbf{S}}_{\mathbf{g}kl}(\tilde{\omega}) \exp[\mathrm{i}\tilde{\omega}(\tau_2 - \tau_1)] \, \mathrm{d}\tilde{\omega} \tag{28}$$

The PSD matrix $\hat{\mathbf{S}}_{\mathbf{g}}(\omega)$ of all axle loads is a $3n_a \times 3n_a$ matrix which is calculated by means of Eqs. (17) and (18):

$$\hat{\mathbf{S}}_{\mathbf{g}}(\omega) = \{[\hat{\mathbf{C}}^t(\omega) + \hat{\mathbf{C}}^v(\omega)]^{-1}\hat{\mathbf{T}}(\omega) \otimes [\hat{\mathbf{C}}^t(\omega) + \hat{\mathbf{C}}^v(\omega)]^{-1*}\hat{\mathbf{T}}(\omega)^*\} \frac{1}{v} \tilde{S}_{rzz}\left(-\frac{\tilde{\omega}}{v}\right) \tag{29}$$

Introducing Eq. (28) in Eq. (27) leads to:

$$\begin{aligned} \mathbf{R}_{\mathbf{u}}(y, t_1, t_2) = \int_{-\infty}^{+\infty} \sum_{k=1}^{n_a} \sum_{l=1}^{n_a} \Bigg[& \int_{-\infty}^{t_1} \mathbf{H}^{\mathrm{T}}(y - y_{k0} - v\tau, t_1 - \tau_1) \exp(-\mathrm{i}\tilde{\omega}\tau_1) \, \mathrm{d}\tau_1 \\ & \otimes \int_{-\infty}^{t_2} \mathbf{H}^{\mathrm{T}}(y - y_{l0} - v\tau, t_2 - \tau_2) \exp(\mathrm{i}\tilde{\omega}\tau_2) \, \mathrm{d}\tau_2 \Bigg] : \hat{\mathbf{S}}_{\mathbf{g}kl}(\tilde{\omega}) \, \mathrm{d}\tilde{\omega} \end{aligned} \tag{30}$$

Comparison of the integral with respect to τ_1 with Eq. (4) shows that this is a matrix with three columns that each represent the response at a point $\{x, y, z\}^{\mathrm{T}}$ due to a harmonic moving load with a time history $\exp(\mathrm{i}\tilde{\omega}t)$ at a position $\{x, y_{k0} + vt, z\}^{\mathrm{T}}$. Therefore, this matrix is the time-domain representation $\mathbf{U}^{\mathrm{T}}(y - y_{k0}, t, \tilde{\omega})$ of the matrix $\hat{\mathbf{U}}^{\mathrm{T}}(y - y_{k0}, \omega, \tilde{\omega})$ introduced in Eq. (25). Eq. (30) is now rewritten as:

$$\mathbf{R}_{\mathbf{u}}(y, t_1, t_2) = \int_{-\infty}^{+\infty} \sum_{k=1}^{n_a} \sum_{l=1}^{n_a} [\mathbf{U}^{\mathrm{T}}(y - y_{k0}, t_1, \tilde{\omega}) \otimes \mathbf{U}^{\mathrm{T}*}(y - y_{l0}, t_2, \tilde{\omega})] : \hat{\mathbf{S}}_{\mathbf{g}kl}(\tilde{\omega}) \, \mathrm{d}\tilde{\omega} \tag{31}$$

An evaluation of the right-hand side for $t_1 = t_2$ allows for the computation of the instantaneous running rms value of the response.

A similar expression is obtained for the power spectrum $\mathbf{S}_{\mathbf{u}}(y, \omega_1, \omega_2)$ [m^2/(rad/s)^2] of the response:

$$\mathbf{S}_{\mathbf{u}}(y, \omega_1, \omega_2) = \frac{1}{4\pi^2} \int_{-\infty}^{+\infty} \sum_{k=1}^{n_a} \sum_{l=1}^{n_a} [\hat{\mathbf{U}}^{\mathrm{T}}(y - y_{k0}, \omega_1, \tilde{\omega}) \otimes \hat{\mathbf{U}}^{\mathrm{T}*}(y - y_{l0}, \omega_2, \tilde{\omega})] : \hat{\mathbf{S}}_{\mathbf{g}kl}(\tilde{\omega}) \, \mathrm{d}\tilde{\omega} \tag{32}$$

where the mean square value of the modulus is obtained for $\omega_1 = \omega_2$. Sheng et al. [12] add the power spectrum of the quasi-static response to the power spectrum of the dynamic response in Eq. (32) to evaluate the total power spectrum of vibrations induced by running trains.

In the double summations in Eqs. (31) and (32), the terms where $k \neq l$ account for the cross-correlation between the dynamic loads at two axles k and l. In the present case, where all axles experience the same track unevenness, these terms are different from zero. In the time domain, however, a good approximation of the mean square response is obtained when the cross-correlation is neglected. In the frequency domain, cross-correlation results in the modulation of the response that has been discussed in Section 2.2. If cross-correlation is neglected or, equivalently, if unevenness perceived by different axles is not correlated, the response in the frequency domain is smoothed out, as pointed out by Hunt [48] for the similar problem of wheel-base filtering in the case of road traffic.

In the following, these mean square response quantities are referred to as ensemble averages, as they represent an average that would be obtained from train passages on several samples of unevenness. If ergodic samples of track unevenness are considered, the same average is obtained if the response along a single track is considered.

Comparing Eq. (32) for the ensemble average with Eq. (24) for a single sample shows that, after discretization with respect to $\tilde{\omega}$, both expressions require the computation of the matrix $\hat{\mathbf{U}}^{\mathrm{T}}(y - y_{k0}, \omega, \tilde{\omega}_m)$ that collects the response due to a series of moving harmonic loads at frequencies $\tilde{\omega}_m$. The computational cost of both expressions is therefore similar.

3. The influence of the train speed in numerical predictions

3.1. Dynamic characteristics of the track and the soil

In 2002, vibration measurements have been performed during homologation tests of the high-speed line L2 between Brussels and Köln [49]. At the measurement site in Lincent (Belgium), 11 passages of the Thalys HST at speeds between 218.1 and 326.1 km/h have been measured and 11 passages of the InterCity train with speeds between 155.9 and 225.3 km/h. Recently, data of two passages of the Thalys HST have been used to validate a numerical model for the prediction of free-field vibrations due to railway traffic [16].

The track in Lincent is a classical ballasted track with UIC 60 rails supported every 0.60 m by rubber pads on monoblock concrete sleepers. The rails are continuously welded and are fixed with a Pandrol E2039 rail fastening system and supported by resilient studded rubber rail pads (type 5197) with a thickness of 11 mm. Each rail pad is preloaded with a clip toe load of about 20 kN per rail seat. The prestressed concrete monoblock sleepers have a length $l_{\mathrm{sl}} = 2.50\,\mathrm{m}$, a width $b_{\mathrm{sl}} = 0.235\,\mathrm{m}$, a height $h_{\mathrm{sl}} = 0.205\,\mathrm{m}$ (under the rail) and a mass $m_{\mathrm{sl}} = 300\,\mathrm{kg}$. The track is supported by a porphyry ballast layer (calibre 25/50, thickness $d = 0.35\,\mathrm{m}$) and a limestone sub-ballast layer (thickness $d = 0.60\,\mathrm{m}$). The density of these ballast layers is $1700\,\mathrm{kg/m^3}$. A rail receptance test has been performed [50] to determine the dynamic characteristics of the rail pads and the ballast [16]. Furthermore, the transfer functions between the track and the free field [53] have been measured as well.

Borings that have been performed before the construction of the high-speed line show that the soil consists of a shallow quaterny top layer of silt with a thickness of 1.2 m, followed by a layer of fine sand upto a depth of 3.2 m. Between 3.2 and 7.5 m is a sequence of stiff layers of arenite (a sediment of a sandstone residue) embedded in clay. Below the arenite layers is a layer of clay (from 7.5 to 8.5 m depth), followed by fine sand (from 8.5 to 10.0 m), below which thin layers of fine sand and clay are found. Below the ballast, the soil has been mixed with lime to improve its mechanical properties. The dynamic soil characteristics have been determined by means of two spectral analysis of surface wave (SASW) tests [51] and five seismic cone penetration tests (SCPT) [52]. These results show that the soil can be represented by a single layer with a thickness of 3.0 m and a shear wave velocity between 150 and 160 m/s on top of a half-space with a shear wave velocity between 250 and 280 m/s [51]. A value of 0.03 has been estimated for the material damping ratio β in deviatoric and volumetric deformatio by fitting measured and predicted transfer functions between the track and the free field. Furthermore, a value of 1/3 has been assumed for the Poisson's ratio and a density ρ equal to $2000\,\mathrm{kg/m^3}$.

In the following, numerical predictions are used to evaluate the quasi-static and dynamic contribution to the track and free-field response during a train passage. The numerical predictions are compared with the field measurements during the homologation tests. The highest train speed during the tests is 330 km/h and is approximately half the value of the shear wave velocity in the top layer of the soil. It can therefore be assumed that all train speeds are well below the critical velocity of the coupled system. An exceedance of the critical velocity is only encountered in the relatively rare case where high-speed tracks are supported by a very soft soil [1,2].

The numerical predictions are obtained by means of an equivalent longitudinally invariant track model. The dynamic characteristics of the track and the soil have been determined by means of the aforementioned in situ tests. The reader is referred to a recent journal paper [16] for more details about the model and the determination of the parameters of the model. In order to better appreciate the results in the following subsections, however, the response of the sleeper due to a unit impulse on the rail and the mobility in the free field at 16 m from the track are briefly recapitulated here. Fig. 2a compares the predicted and measured response of the sleeper below the point of impact on the rail in a frequency range upto 400 Hz. The peak near 25 Hz is due to the soil stratification, where a relatively soft layer overlays a stiffer half-space. The resonance frequency of the rail on the rail pad is approximately 350 Hz and is not observed in the sleeper response. Although a discrepancy is observed between measured and predicted results in the low-frequency range, the overall correspondence is relatively good. Fig. 2b shows the mobility in the free field at 16 m from the track upto 150 Hz. Both curves show an increasing mobility at low frequencies, decreasing values at frequencies above 60 Hz and a maximum at intermediate frequencies between 10 and 60 Hz. The overestimation of the mobility at high frequencies might be due to a wrong estimation of the material damping ratio that has a large influence in a broad range of frequencies at large distances.

3.2. Dynamic train characteristics

The high-speed train on the high-speed line L2 between Brussels and Köln is an articulated Thalys PBKA train with two locomotives and eight carriages. It has a total length of 200.18 m. The carriage length L_t, the distance L_b between bogies, the axle distance L_a, the total axle mass M_t, the sprung axle mass M_s and the unsprung axle mass M_u of all carriages are summarized in Table 1.

The InterCity train consists of a locomotive HLE13, seven standard central HVI11 coaches and one back coach HV I11 BDx. Table 2 summarizes the train characteristics.

3.3. Track unevenness

The track unevenness at the measurement site has been measured shortly before the homologation tests with the EM-130 track recording car of the Belgian railway company NMBS [54]. The measured unevenness has been used to derive a one-sided PSD in the range of wavelengths between 6 and 24 m. For a train speed of 330 km/h, which is the highest speed during the homologation tests, this range of wavelengths corresponds to an excitation of the vehicle's axles in the frequency range between 3.8 and 15.3 Hz. For lower train speeds, the frequency range is even lower. For an accurate prediction of the dynamic axle loads in a frequency range between 1 and 150 Hz, complementary data on the unevenness in the range of wavelengths between 0.3 and 6 m and the range between 24 and 100 m are required for train speeds between 150 and 330 km/h. However, as such data were not available, the measured PSD has been fitted by the following PSD [m^2/(rad/m)]:

$$\tilde{S}_{rzz}(k_y) = \tilde{S}_{rzz}(k_{y0})\left(\frac{k_y}{k_{y0}}\right)^{-n} \tag{33}$$

with $k_{y0} = 1$ rad/m. A value of 3.5 has been chosen for n, in agreement with values between 3 and 4 reported by Braun and Hellenbroich [55] for railway unevenness. It is therefore assumed that, on a double logarithmic

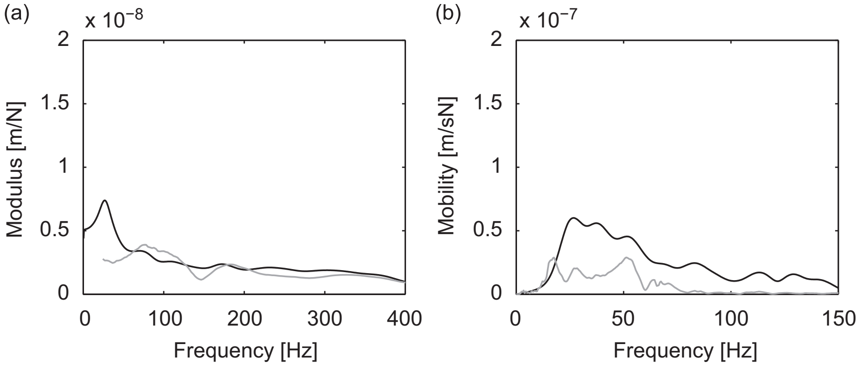

Fig. 2. Measured (grey line) and predicted (a) response of the sleeper due to a unit impulse on the rail and (b) mobility in the free field at 16 m from the track.

Table 1
The Thalys HST

	Axles (dimensionless)	L_t (m)	L_b (m)	L_a (m)	M_t (kg)	M_s (kg)	M_u (kg)
2 Locomotives	4	22.15	14.00	3.00	17,000	14,937	2027
2 Side coaches	3	21.84	18.70	3.00	17,000	14,937	2027
3 Central coaches	2	18.70	18.70	3.00	17,000	14,937	2027

Table 2
The InterCity train

	Axles (dimensionless)	L_t (m)	L_b (m)	L_a (m)	M_t (kg)	M_s (kg)	M_u (kg)
Locomotive HLE13	4	19.11	10.40	3.00	22,500	19,677	2823
Central coach HVI11 A	4	26.40	18.40	2.56	11,610	10,100	1500
Central coach HVI11 B	4	26.40	18.40	2.56	11,602	10,102	1500
End coach HV I11 BDx	4	26.40	18.40	2.56	11,830	10,286	1544

scale, the PSD function has the same slope in the entire range of wavelengths that is considered in the predictions. This is not necessarily the case, as the track unevenness in different ranges of wavelengths results from different physical phenomena. In the present case, however, insufficient data are available to fit a more elaborate model for the track unevenness. The fit leads to a value of $1.36 \times 10^{-8}\,\mathrm{m}^2/(\mathrm{rad/m})$ for $\tilde{S}_{rzz}(k_{y0})$.

In the numerical predictions, a single sample $u_{rz}(y)$ of track unevenness is generated from the PSD by means of Eq. (20). The spatial sampling is chosen such that, for each train speed, a sufficiently long and densely sampled stretch of unevenness is obtained. Therefore, $\Delta y = v_{\min}\Delta t$ and $Y = 2v_{\max}T$, where $v_{\min}$ and $v_{\max}$ are the minimum and maximum train speed considered. For each speed, a stretch of $u_{rz}(y)$ with the appropriate length is chosen and resampled at $\Delta y = v\Delta t$, taking appropriate measures for anti-aliasing. A Hanning window is applied to avoid leakage.

In the following, the influence of the train speed is investigated by means of numerical predictions of the dynamic axle loads and the track and free-field response. A distinction is made between the quasi-static and dynamic excitation. Two passages of both the Thalys HST and the InterCity train are considered. The two speeds for each train type are the maximum and minimum value that have been measured during the homologation tests. Next, the scatter between predictions for different samples of track unevenness generated from the same PSD is discussed for a single passage of the Thalys HST. The results for these samples are compared with ensemble average quantities. Finally, measured and predicted one-third octave band spectra and running rms values of the track and free-field velocity are compared for different train speeds.

3.4. *The quasi-static response for a single axle of the locomotive*

The quasi-static response due to the passage of a single axle of the InterCity train and the Thalys HST is calculated by means of Eq. (11). Figs. 3a and c show the frequency content of the sleeper velocity due to the passage of the first axle of the locomotive of the InterCity train at a speed of 156 and 224 km/h, respectively. At the highest speed, a shift to higher frequencies is observed. Figs. 4a and c show the corresponding time history of the sleeper velocity. The sleeper velocity has a single upward and downward peak, as can be expected from the time history of the track deflection. At higher train speeds, the response is shorter in time and the peak particle velocity (PPV) increases. Figs. 3b and d and 4b and d show similar results for the passage of the first axle of the locomotive of the Thalys HST at a speed of 218 and 307 km/h, respectively. As the train speed in Figs. 3b and c is very similar, the difference between both results is only due to the slightly higher total axle weight of the locomotive of the InterCity train (Tables 1 and 2).

The quasi-static response for the complete train is obtained from Eq. (11) by multiplication of the frequency content of the response due to a single axle (Fig. 3) and the train spectrum (Fig. 5). Figs. 5a and c show the spectrum for both passages of the InterCity train. The spectrum is quasi-discrete and shows multiple peaks. These peaks correspond to multiples of fundamental bogie passage frequencies $f_b = v/L_b$ and axle passage frequencies $f_a = v/L_a$ [29,37,38]. A higher train speed shifts this spectrum to higher frequencies and does not affect its amplitude. Figs. 5b and d show the spectrum for the two speeds of the Thalys HST and show a similar shift with the train speed. In Section 3.6, the quasi-static response of the complete train will be calculated and added to the dynamic response. The quasi-static response in the free field is not considered here, as the results in Section 3.6 will show that it can be neglected compared with the dynamic response.

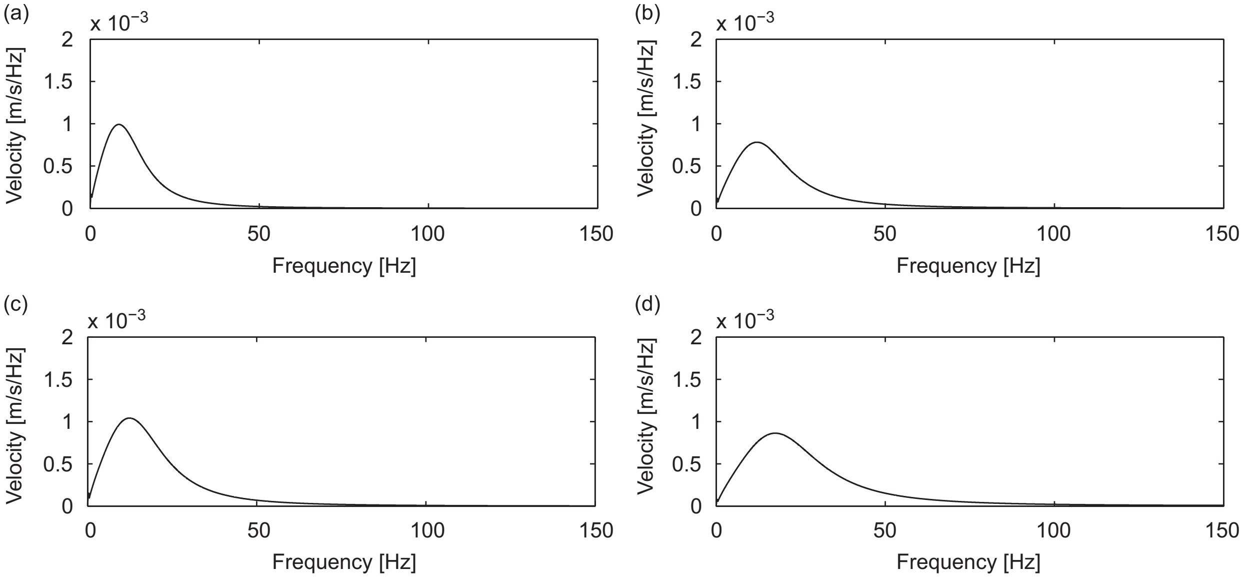

Fig. 3. Frequency content of the quasi-static sleeper velocity due to the passage of the first axle of the locomotive for (a) an InterCity train at 156 km/h, (b) a Thalys HST at 218 km/h, (c) an InterCity train at 224 km/h and (d) a Thalys HST at 307 km/h.

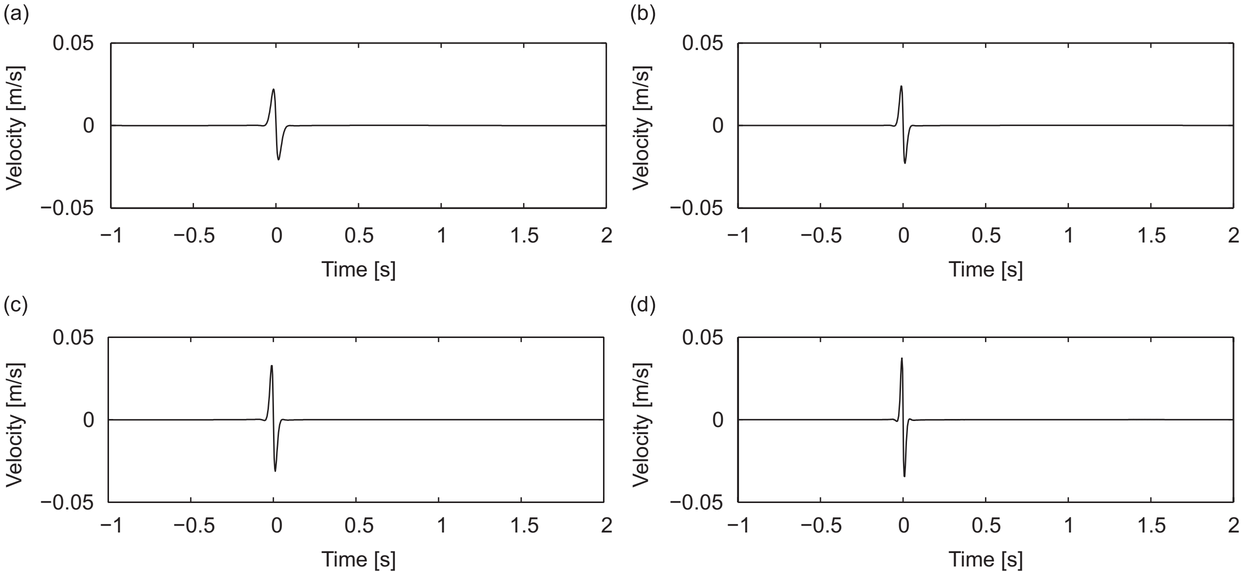

Fig. 4. Time history of the quasi-static sleeper velocity due to the passage of the first axle of the locomotive for (a) an InterCity train at 156 km/h, (b) a Thalys HST at 218 km/h, (c) an InterCity train at 224 km/h and (d) a Thalys HST at 307 km/h.

3.5. The dynamic response for a single axle

Prior to the calculation of the track and the free-field response due to dynamic excitation, the dynamic axle loads are calculated according to Eq. (17). The track compliance matrix is calculated in a moving frame of reference according to Eq. (14). At frequencies of more than a few Hertz [3], the vehicle's primary and secondary suspension isolate the body and the bogie from the wheelset. The vehicle compliance matrix $\hat{\mathbf{C}}^{v}(\omega)$ is therefore a diagonal matrix $\hat{\mathbf{C}}^{v}(\omega) = \text{diag}\{-1/(M_{uk}\omega^{2})\}$ that only takes into account the inertia of the unsprung mass of the train axles (Tables 1 and 2).

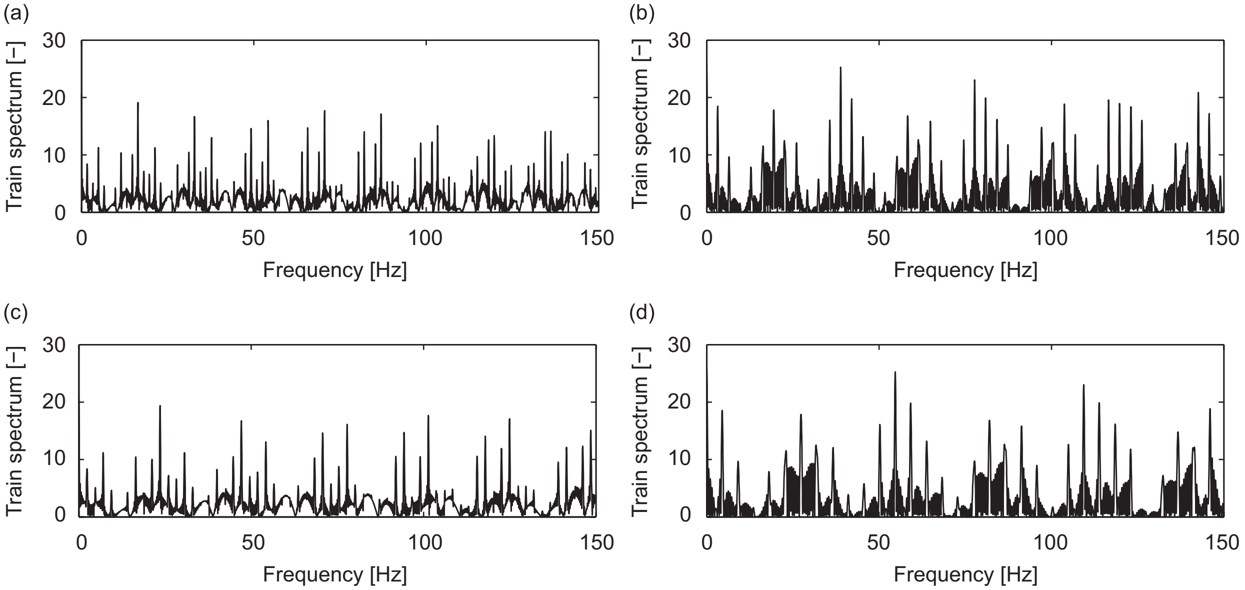

Fig. 5. Modulation of the frequency content of the quasi-static response for (a) an InterCity train at 156 km/h, (b) a Thalys HST at 218 km/h, (c) an InterCity train at 224 km/h and (d) a Thalys HST at 307 km/h.

Fig. 6 shows the first diagonal element of the dynamic stiffness matrix $[\hat{\mathbf{C}}^t(\omega) + \hat{\mathbf{C}}^v(\omega)]^{-1}$ of the coupled train–track system that relates the frequency content of the dynamic load at the first axle of the locomotive to the unevenness perceived by the same axle. Fig. 6a shows the result for the InterCity train at a speed of 156 km/h. At low frequencies, the dynamic stiffness of the coupled system is dominated by the inertia of the unsprung mass. The real part has a value of approximately $-M_{u1}\omega^2$, while the imaginary part is small. Near 65 Hz, the real part becomes zero and the imaginary part shows a maximum. This corresponds to the resonance of the unsprung mass on the track. The results for a train speed of 156 km/h (Fig. 6a) are only slightly different from those for a speed of 224 km/h (Fig. 6c). This is due to the limited influence of the train speed on the track compliance matrix $\hat{\mathbf{C}}^t(\omega)$ in the subcritical range of train speeds. The dynamic stiffness of the first axle of the Thalys HST (Figs. 6b and d) shows a higher resonance frequency than the InterCity train (Figs. 6a and c) due to the lower unsprung mass of the locomotive 's axle (Tables 1 and 2).

The perceived unevenness in the right-hand side of Eq. (17) is calculated from the sample of unevenness that has been generated by means of Eq. (20) according to the procedure described in Section 3.3. Fig. 7 shows the frequency content of the dynamic load of the first axle of the locomotive of the InterCity train and Thalys HST for both train speeds. For both train types and speeds, a maximum occurs between 40 and 70 Hz that corresponds to the resonance frequency of the unsprung mass on the track. At a similar train speed, the dynamic load of the locomotive of the InterCity train (Fig. 7b) seems slightly higher than for the Thalys HST (Fig. 7c) at frequencies below the resonance frequency and lower at frequencies above. In the following section, the influence of the train speed is investigated by means of one-third octave band spectra of the dynamic loads.

The dynamic load of the first axle of the locomotive (Fig. 7) is now used to calculate the dynamic response of the sleeper in the frequency domain (Fig. 8) by means of Eq. (23). The largest values are observed near the resonance frequency of the unsprung mass on the track. A comparison of Figs. 8a and c or b and d shows that the sleeper velocity slightly increases with increasing train speed. The dynamic sleeper velocity is smaller than the quasi-static velocity (Fig. 3) at low frequencies, but dominates at higher frequencies.

In the time domain (Fig. 9), the dynamic sleeper velocity has a much longer duration than the quasi-static velocity (Fig. 4), as it consists of waves emitted by the moving source, and not of a quasi-static deflection pattern that travels with the source. The PPV of the dynamic response is much smaller than the quasi-static PPV (Fig. 4).

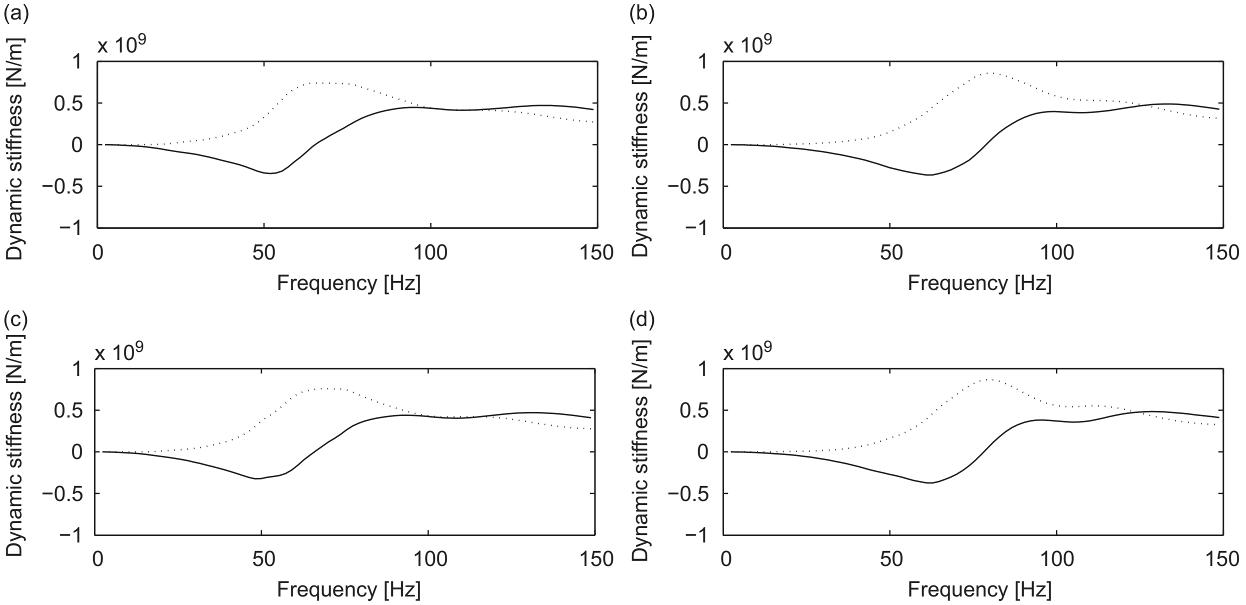

Fig. 6. Real (solid line) and imaginary part (dotted line) of the dynamic stiffness of the first axle of the locomotive coupled to the track for (a) an InterCity train at 156 km/h, (b) a Thalys HST at 218 km/h, (c) an InterCity train at 224 km/h and (d) a Thalys HST at 307 km/h.

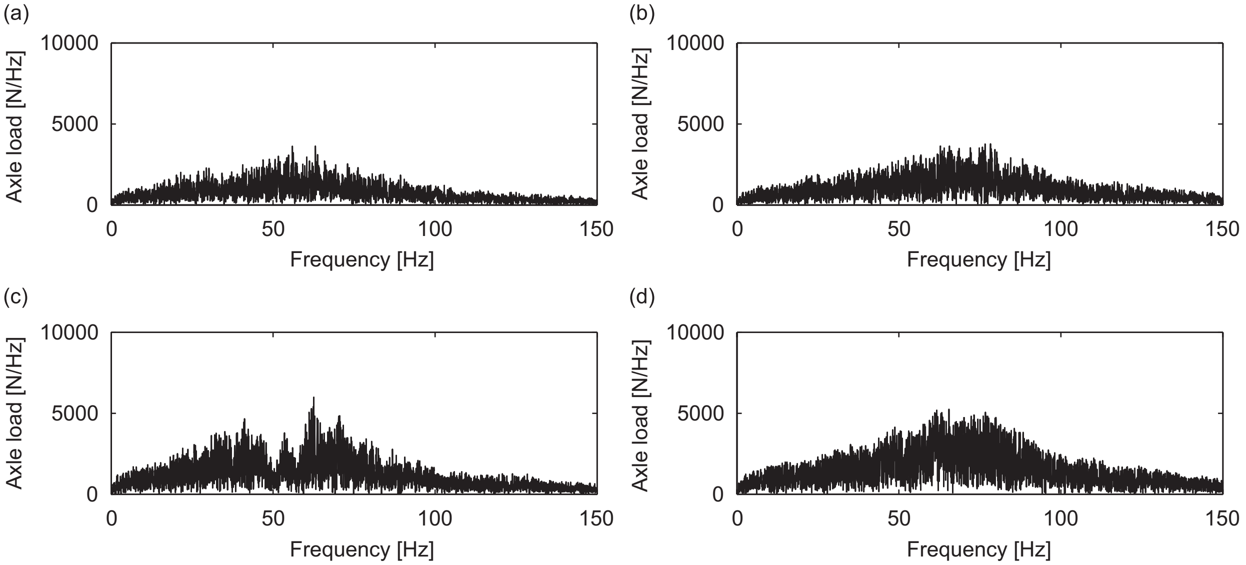

Fig. 7. Frequency content of the dynamic load of the first axle of the locomotive for (a) an InterCity train at 156 km/h, (b) a Thalys HST at 218 km/h, (c) an InterCity train at 224 km/h and (d) a Thalys HST at 307 km/h.

Fig. 10 shows the frequency content of the vertical velocity in the free field at 16 m from the track. As for the sleeper, the frequency content of the velocity is large near the resonance frequency of the unsprung mass on the track. The response at higher frequencies is relatively more attenuated due to material damping in the soil. The increase of the dynamic load with the train speed (Fig. 7) also affects the vibrations in the free-field, so that a slightly higher modulus of the free field velocity is obtained for increasing train speeds.

Fig. 11 shows the time history of the vertical velocity in the free field. Compared with the results for the sleeper (Fig. 9), the maximum is delayed in time due to wave propagation in the soil. At a larger train speed, the PPV slightly increases and the response duration decreases.

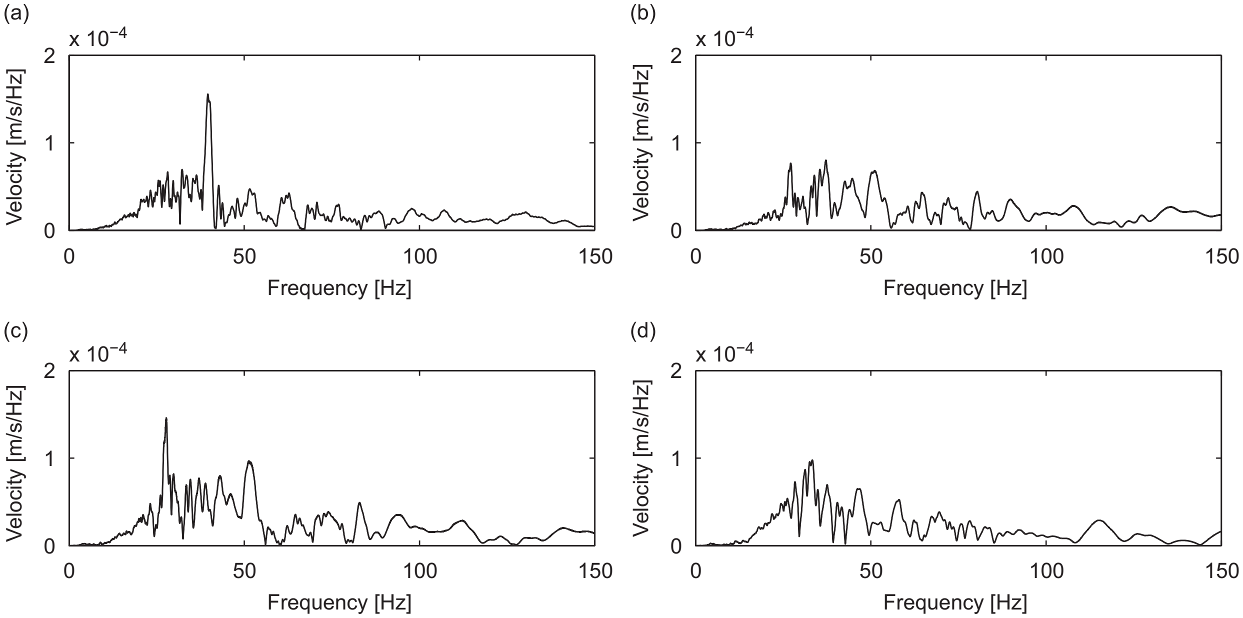

Fig. 8. Frequency content of the dynamic sleeper velocity due to the passage of the first axle of the locomotive for (a) an InterCity train at 156 km/h, (b) a Thalys HST at 218 km/h, (c) an InterCity train at 224 km/h and (d) a Thalys HST at 307 km/h.

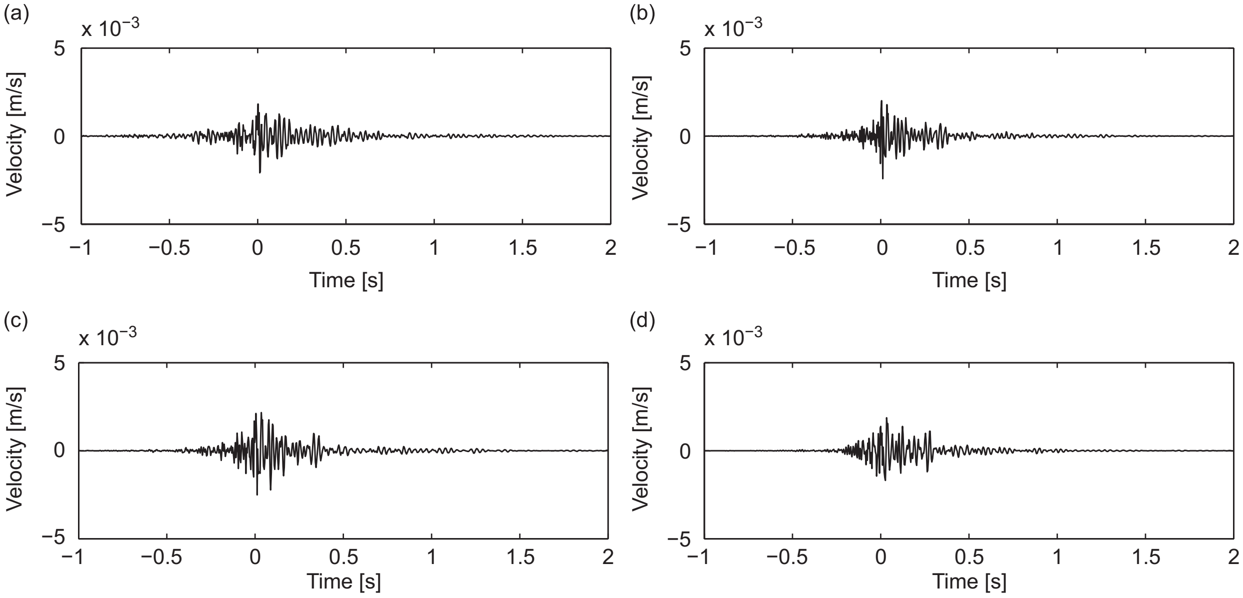

Fig. 9. Time history of the dynamic sleeper velocity due to the passage of the first axle of the locomotive for (a) an InterCity train at 156 km/h, (b) a Thalys HST at 218 km/h, (c) an InterCity train at 224 km/h and (d) a Thalys HST at 307 km/h.

3.6. Quasi-static and dynamic response for the complete train

Fig. 12 shows the frequency content of the sleeper velocity due to the passage of the complete InterCity train and Thalys HST. The response is obtained as the superposition of the quasi-static and dynamic response due to all axles.

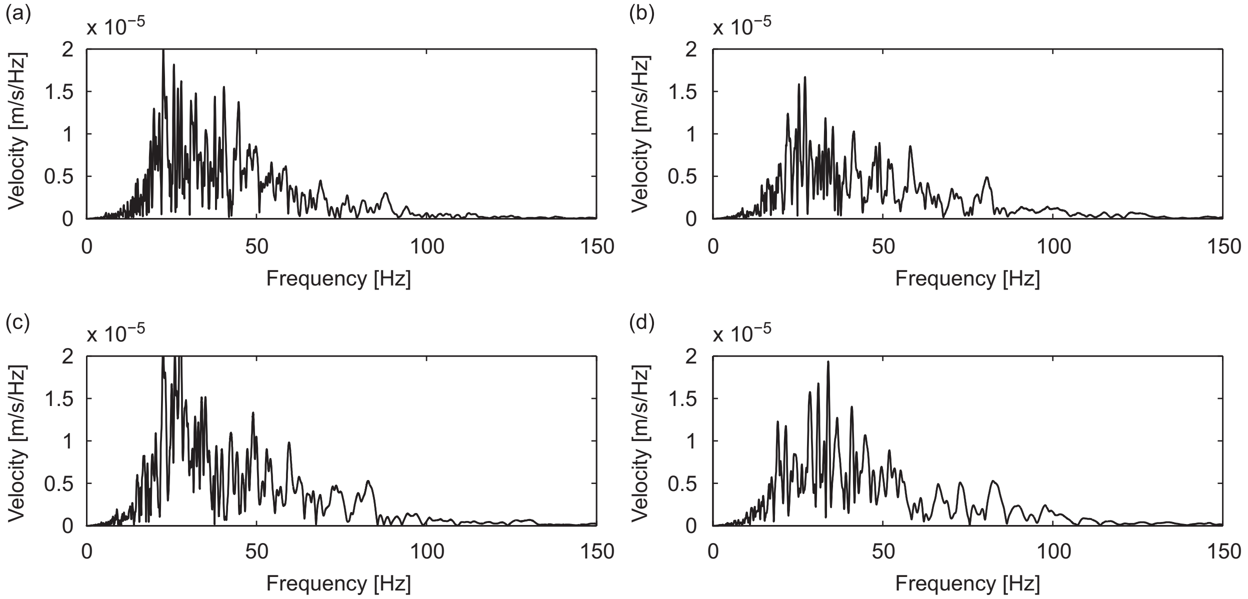

Fig. 10. Frequency content of the dynamic free-field velocity at 16 m from the track due to the passage of the first axle of the locomotive for (a) an InterCity train at 156 km/h, (b) a Thalys HST at 218 km/h, (c) an InterCity train at 224 km/h and (d) a Thalys HST at 307 km/h.

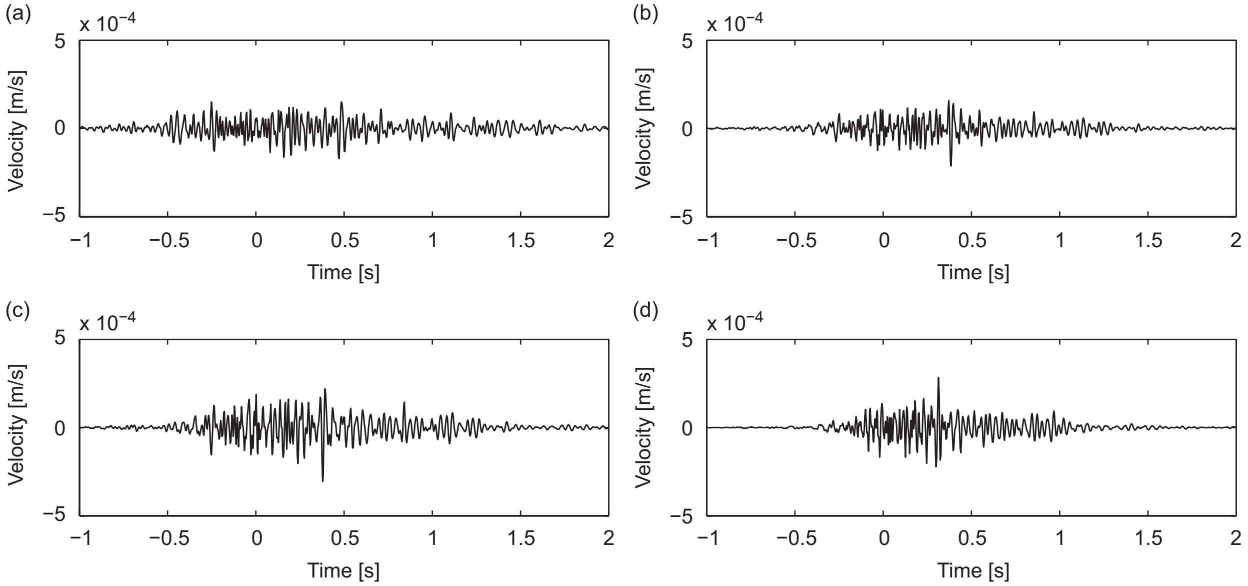

Fig. 11. Time history of the dynamic free-field velocity at 16 m from the track due to the passage of the first axle of the locomotive for (a) an InterCity train at 156 km/h, (b) a Thalys HST at 218 km/h, (c) an InterCity train at 224 km/h and (d) a Thalys HST at 307 km/h.

In order to distinguish between the quasi-static and dynamic contribution to the sleeper velocity, the one-third octave band spectra of the total and dynamic sleeper velocity are computed (Fig. 13) according to the German standard DIN 45672-2 [56]. According to the standard, a reference period T_2 is determined for the total sleeper velocity during which the response is considered to be stationary. The same reference period T_2 has been used to compute the one-third octave band spectra of the dynamic contribution. The quasi-static

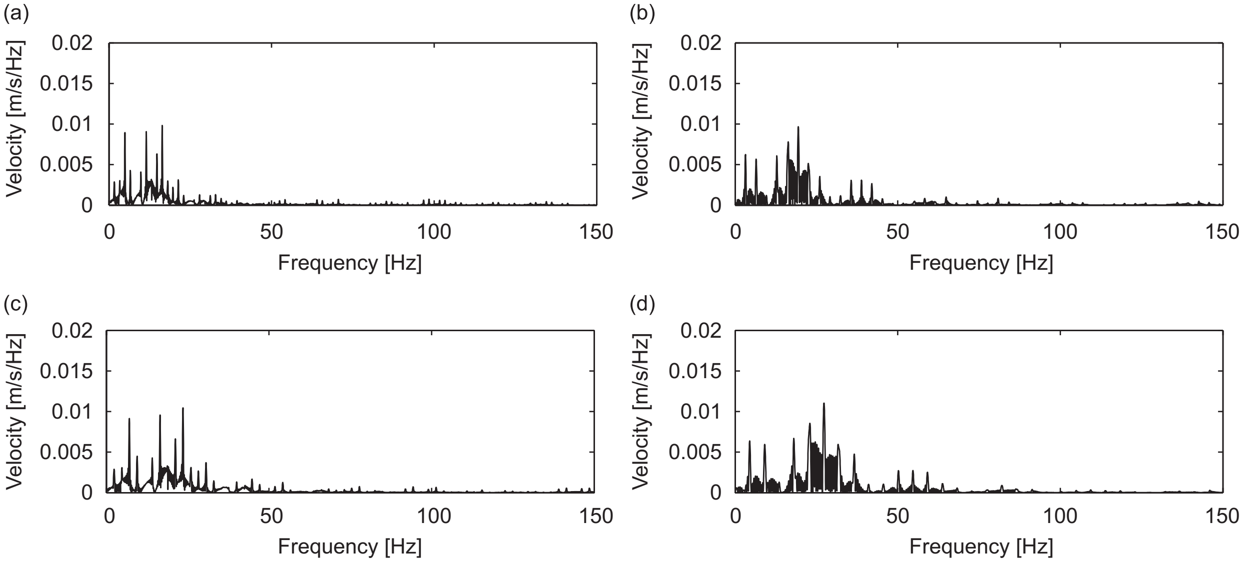

Fig. 12. Frequency content of the sleeper velocity for (a) an InterCity train at 156 km/h, (b) a Thalys HST at 218 km/h, (c) an InterCity train at 224 km/h and (d) a Thalys HST at 307 km/h.

contribution dominates the sleeper velocity in the low-frequency range, where the largest values are found in the one-third octave band spectra. With an increasing train speed, the influence of the quasi-static contribution shifts to higher frequencies.

In the time history of the sleeper velocity (Fig. 14), the passage of individual bogies is recognized. The quasi-static sleeper response due to a single axle (Fig. 9) has a very short duration so that, after superposition, contributions of axles from different bogies do not interfere. In Fig. 14a, the InterCity train is in "pull mode" and the axles of the locomotive that carry the largest weight (Table 2) come first. In Fig. 14c, the InterCity train is in "push mode" and higher velocity levels are observed during the passage of the locomotive at the end of the train. The results for the Thalys HST (Figs. 14b and d) show a similar response for each bogie, as each axle carries the same total weight.

Fig. 15 shows the frequency content of the free-field velocity at 16 m from the track. When the modulation of the frequency content for quasi-static excitation (Fig. 5), the dynamic response due to a single axle (Fig. 10) and the complete response (Fig. 15) are compared, it is observed that the dynamic response also shows a modulation. This is due to the superposition of contributions from different axles with similar magnitude, but different phase, determined by the train speed and axle spacing.

Fig. 16 compares the total and dynamic one-third octave band spectra of the total and dynamic free-field velocity at 16 m from the track. In the free field, the total response is dominated by the dynamic excitation. A significant contribution of the quasi-static excitation to the total response is only found in the low-frequency range below 10 Hz. When the free-field response at 16 m from the track (Fig. 16) is compared with the sleeper response (Fig. 13), it is observed that the dynamic response becomes more important, even in the one-third octave bands at relatively low frequencies. This is can be explained as follows. At subcritical train speeds, the quasi-static response is due to the nearly static deflection around each axle. As the axle moves, the deflections travel with the axle and the displacements at a fixed point in the free field are time dependent. Due to the shape of the deflection bowl, the variation in time becomes slower with increasing distance from the track. As a result, the frequency content of the quasi-static contribution shows a strong shift to lower frequencies with an increasing distance from the track. In the present case, the shift to lower frequencies of the quasi-static response is stronger than the one for the dynamic response, which is due to the material damping in the soil [16].

The results in Fig. 16 show that the lack of agreement between field measurements and predictions of free-field vibrations by Degrande and Lombaert [29] and Paolucci and Spinelli [30] is due to the neglection of the

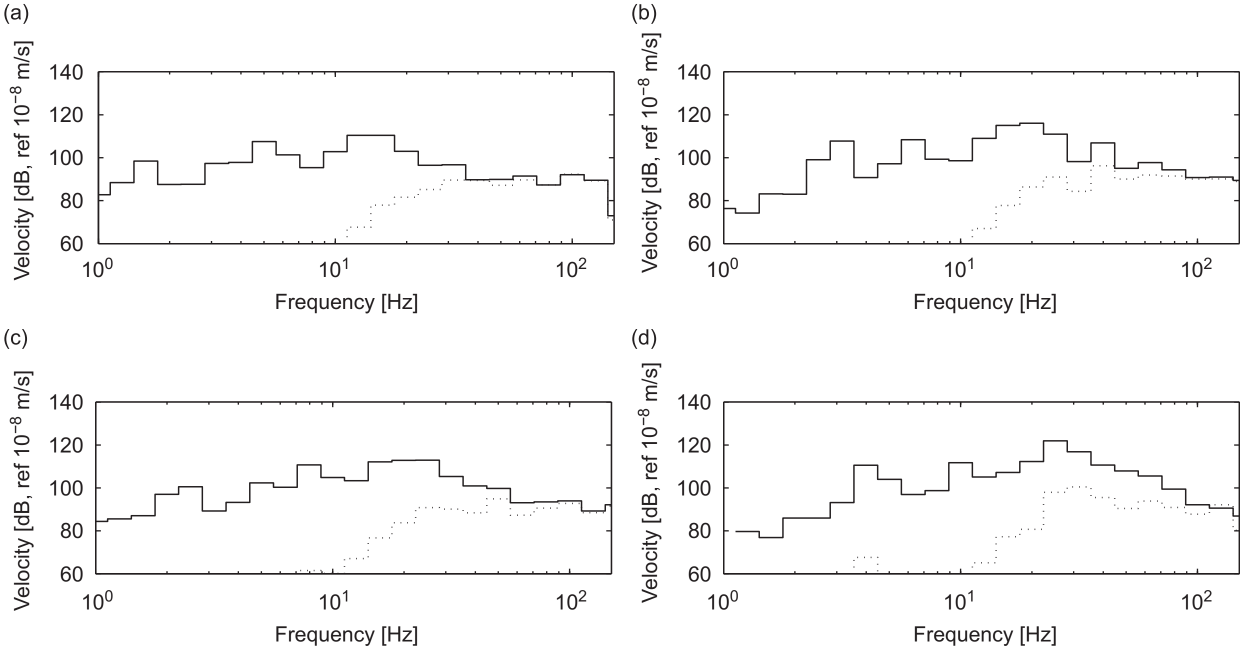

Fig. 13. One-third octave band spectra of the total (solid line) and dynamic (dotted line) sleeper velocity for (a) an InterCity train at 156 km/h, (b) a Thalys HST at 218 km/h, (c) an InterCity train at 224 km/h and (d) a Thalys HST at 307 km/h.

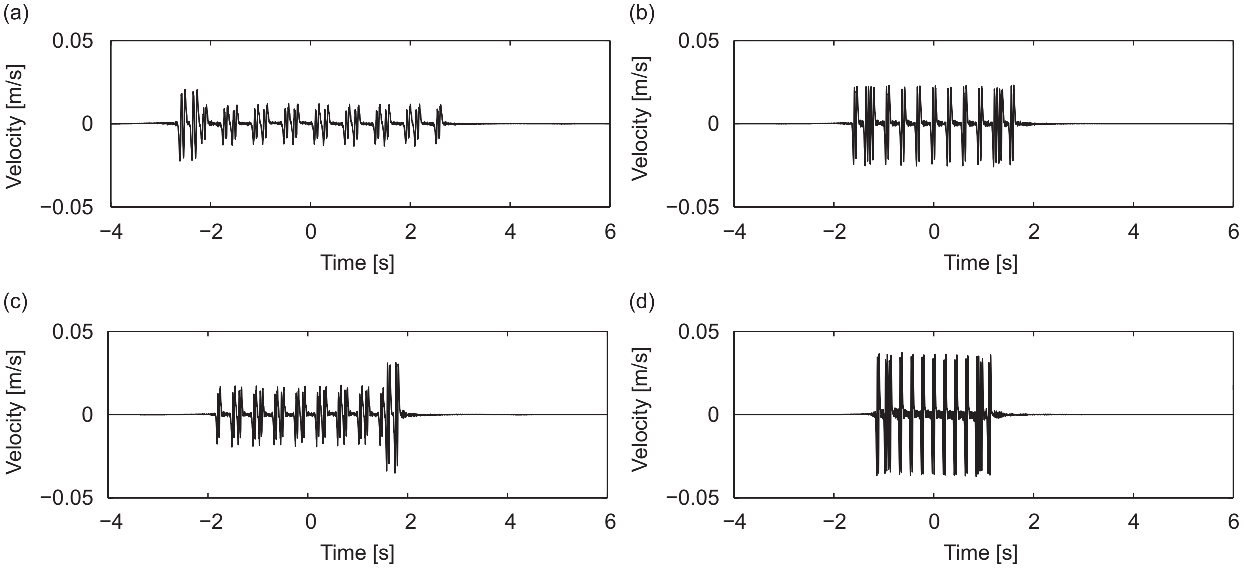

Fig. 14. Time history of the sleeper velocity for (a) an InterCity train at 156 km/h, (b) a Thalys HST at 218 km/h, (c) an InterCity train at 224 km/h and (d) a Thalys HST at 307 km/h.

dynamic excitation. Sheng et al. [11] have studied the importance of the quasi-static and dynamic contributions to the track and free-field response in three case studies. For the case of the X-2000 high-speed train in Ledsgård (Sweden) and train speeds below the critical phase velocity of the coupled track–soil system, similar observations are made. For higher train speeds, however, the quasi-static contribution to the free-field response becomes more important and can no longer be neglected. More results are given in Sheng et al. [12] where several track models are discussed. Auersch [38] has drawn similar conclusions based on measured and

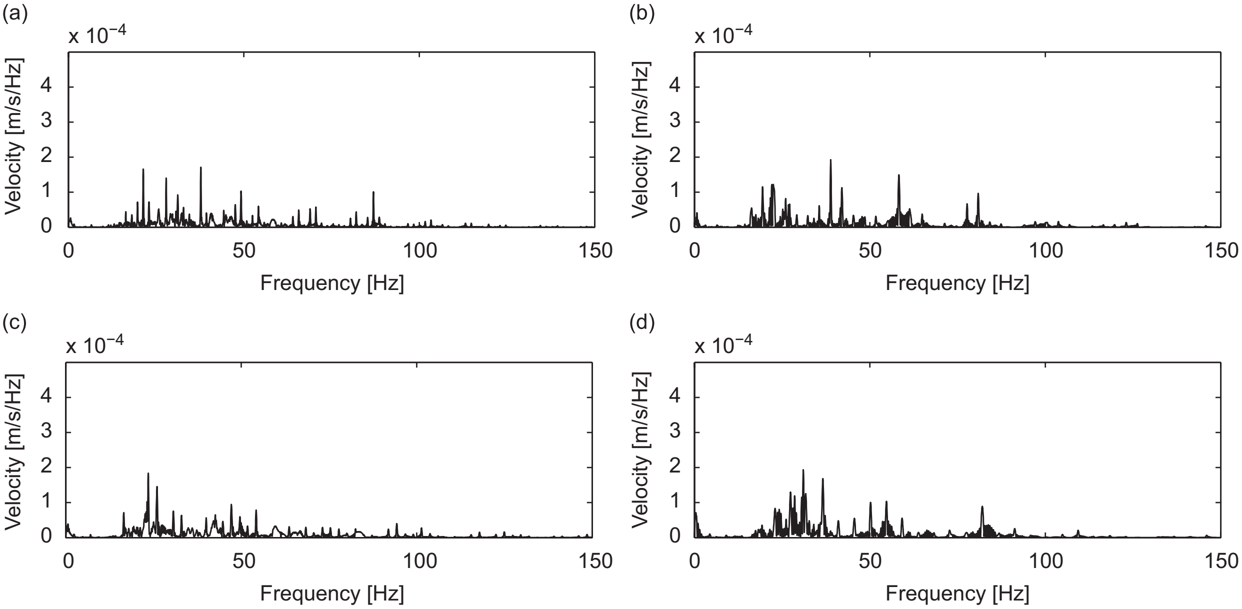

Fig. 15. Frequency content of the free-field velocity at 16 m from the track for (a) an InterCity train at 156 km/h, (b) a Thalys HST at 218 km/h, (c) an InterCity train at 224 km/h and (d) a Thalys HST at 307 km/h.

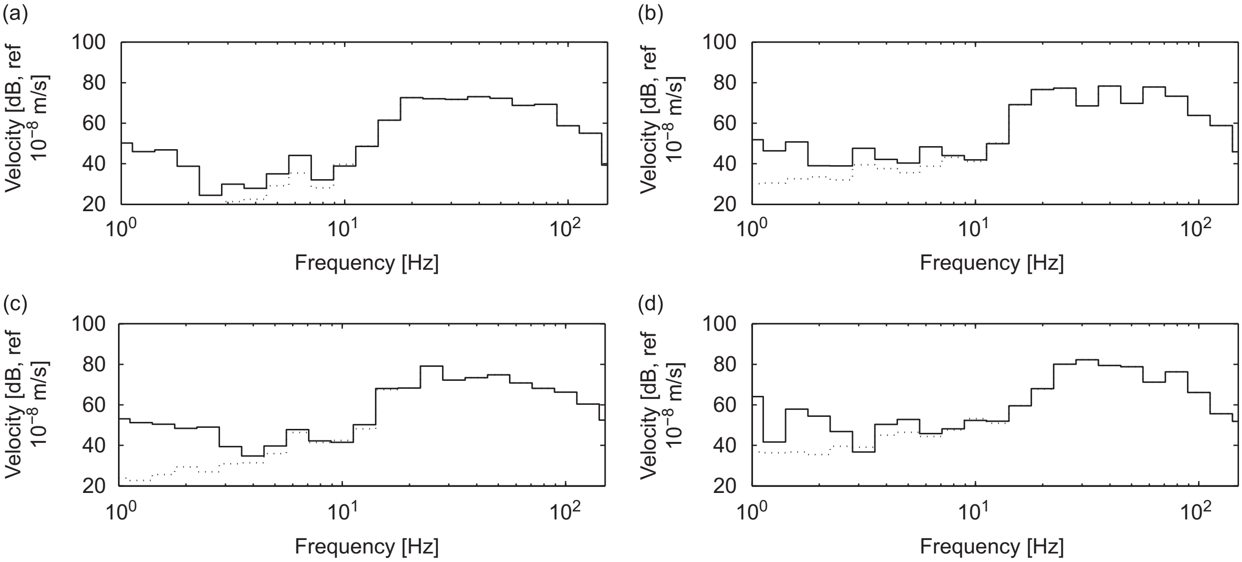

Fig. 16. One-third octave band spectra of the total (solid line) and dynamic (dotted line) free-field velocity at 16 m from the track for (a) an InterCity train at 156 km/h, (b) a Thalys HST at 218 km/h, (c) an InterCity train at 224 km/h and (d) a Thalys HST at 307 km/h.

predicted vibrations for the case of the ICE 3 and Thalys HSTs on the line Berlin-Hannover. In the case of HSTs in the subcritical speed range, predictions of vibrations based on Krylov's model [57,58], such as those recently presented by Degrande and Lombaert [29], Takemiya [59], Paolucci and Spinelli [30] and Galvín and Domínguez [60,31], are therefore only well suited to predict the response in the immediate vicinity of the track.

Fig. 17 shows the time history of the free-field velocity at 16 m from the track. Contrary to the sleeper response in Fig. 14, the passage of individual bogies is no longer observed. The dynamic response for a single axle (Fig. 11) has a longer duration, so that contributions of axles from different bogies overlap in Fig. 17. The results in Figs. 17a and c for the InterCity train suggest a slightly higher response during the passage of the

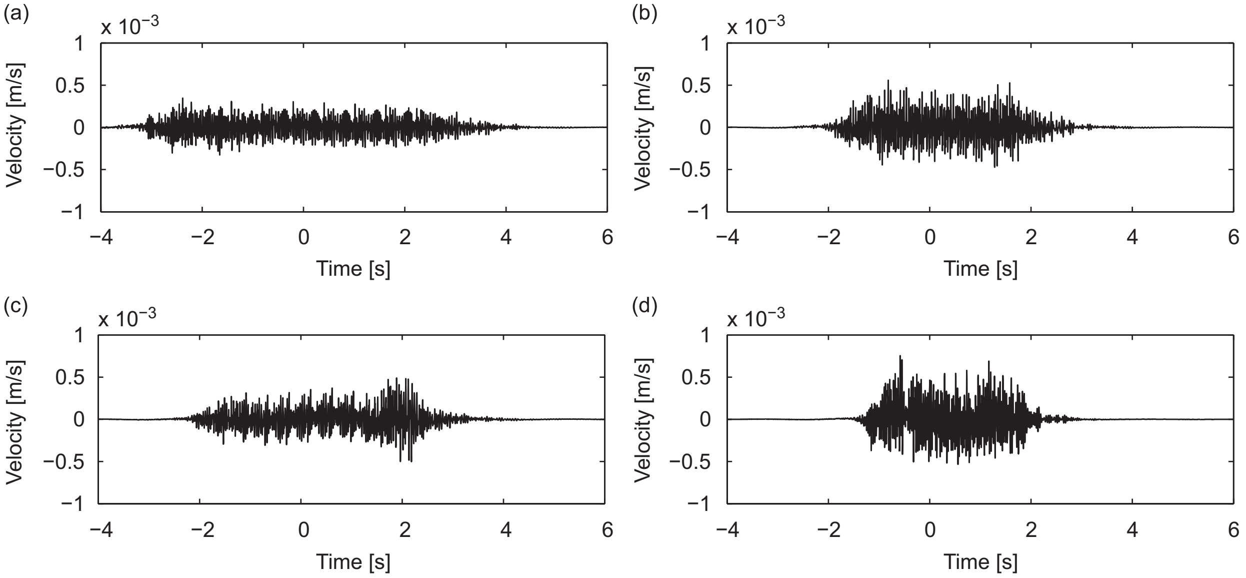

Fig. 17. Time history of the free-field velocity at 16 m from the track for (a) an InterCity train at 156 km/h, (b) a Thalys HST at 218 km/h, (c) an InterCity train at 224 km/h and (d) a Thalys HST at 307 km/h.

locomotive, where the axles have a higher unsprung mass. For similar train speeds, the vibration levels during the passage of the InterCity train (Fig. 17c) and the Thalys HST (Fig. 17b) are similar.

3.7. Variation due to unevenness sampling

In Section 2.4, it has been discussed how different samples of track unevenness yield different predictions of the track and free-field response. The track and free-field response due to a passage of the Thalys HST at a speed of 218 km/h are now calculated for 6 samples of track unevenness $u_{rz}(y)$. The results are compared with the mean square response as computed by means of Eqs. (31) and (32).

The 6 samples of unevenness are generated by means of Eq. (20) as a superposition of harmonic functions with the same amplitude, but a different random phase. Therefore, their one-third octave band spectra (Fig. 18a) coincide, as well as the one-third octave band spectra of the dynamic load of the first axle of the locomotive (Fig. 18b).

Fig. 19 shows the one-third octave band spectrum and running rms value of the sleeper velocity during the passage of the Thalys HST at 218 km/h for all samples. A substantial difference between the one-third octave band spectra (Fig. 19a) only appears in the high-frequency range, where the sleeper response is due to dynamic excitation. Fig. 19b shows the running rms value of the sleeper velocity, computed with a time window of 1 s as prescribed by the ISO 2631 standard [61]. The results for the running rms value almost coincide as the quasi-static contribution dominates the sleeper response.

In Section 2.5, a procedure for the calculation of the ensemble average response due to dynamic excitation has been discussed. Fig. 20a shows the one-third octave band spectrum of the ensemble average sleeper velocity in the frequency domain according to Eq. (32). As no stationary part of the time history is selected for the calculation of the one-third octave band spectra, the values depend on the time period T in the calculation and cannot be compared in absolute terms to the results in Fig. 19a. A quantitative result of the one-third octave band spectrum is obtained as follows. First, the square modulus of the quasi-static sleeper velocity is added to the mean square modulus of the dynamic contribution. Second, the one-third octave band representation of this spectrum is scaled with $\sqrt{T_2/T}$, where T is the time period in the calculation and T_2 is the reference period according to the DIN 45672-2 standard. The resulting one-third octave band spectrum in Fig. 20c compares both qualitatively and quantitatively very well with the previous spectra for the 6 samples in Fig. 19a.

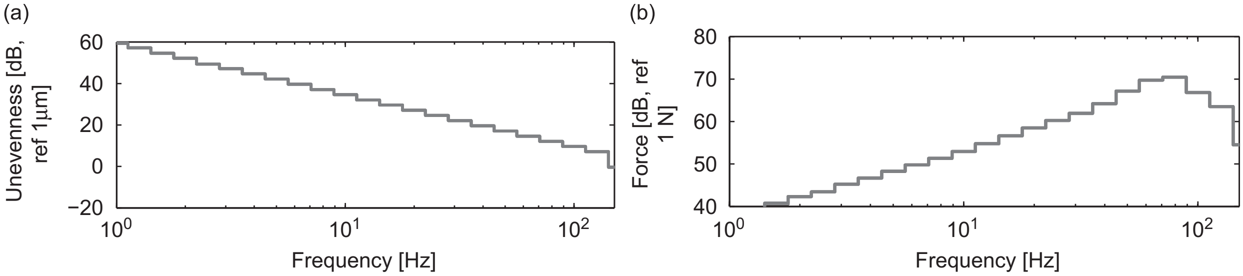

Fig. 18. (a) One-third octave band spectra of 6 samples of vertical track unevenness and (b) the corresponding one-third octave band spectra of the dynamic load of the first axle of the locomotive of the Thalys HST for a train speed of 218 km/h.

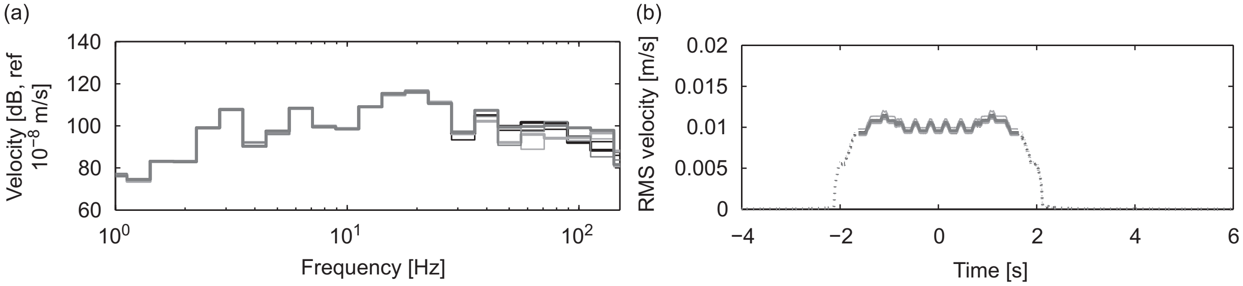

Fig. 19. (a) One-third octave band spectra and (b) running rms value of the sleeper velocity due to a passage of the Thalys HST at a speed v of 218 km/h for 6 samples of vertical track unevenness. The dotted and solid line in (b) show the running rms value outside and during the DIN 45672-2 reference period T_2, respectively.

The reference period T_2 for the scaling of the one-third octave band spectra has been determined from the total instantaneous rms value of the sleeper velocity. This value is obtained as the root of the sum of the square quasi-static response and the mean square dynamic response (Fig. 20c) according to Eq. (31). The total instantaneous rms value has been used to compute the total running rms value with a time window of 1 s (Fig. 20d). Due to the small dynamic contribution to the sleeper response, the result in Fig. 19b is very similar for all samples.

Fig. 21a shows the one-third octave band spectrum of the free-field velocity at 16 m from the track for all samples. Contrary to the results for the sleeper, differences upto 10 dB are now observed in the entire frequency range. The running rms values of the free-field velocity (Fig. 21b) differ upto a factor of 2. Due to ergodicity, this means that, even when the track unevenness has stationary statistical characteristics, substantial differences are expected between vibration levels in the free-field along a railway line. It would therefore be interesting to verify the variability of the free-field response along the track with an experimental setup as used by Ditzel et al. [35].

Fig. 22a shows the unscaled ensemble average one-third octave band representation of the free-field velocity at 16 m from the track due to dynamic excitation. In a similar way as for the sleeper, the one-third octave band spectrum of the total free-field velocity is obtained (Fig. 22c). This gives a good estimate of the one-third octave band spectra for actual samples of unevenness (Fig. 21a). The instantaneous running rms value of the dynamic response (Fig. 22b) has been used to calculate the running rms value of the total response (Fig. 22d) with a time window of 1 s. Although only 6 samples are considered in Fig. 21b, their average corresponds well to the ensemble average.

4. Comparison of predictions and field measurements

4.1. One-third octave band spectra of the vibration velocity for two train speeds

Before comparing numerical predictions and measured data of the response during a train passage, the one-third octave band spectra of perceived track unevenness are shown (Fig. 23). In Fig. 23a, the train speed

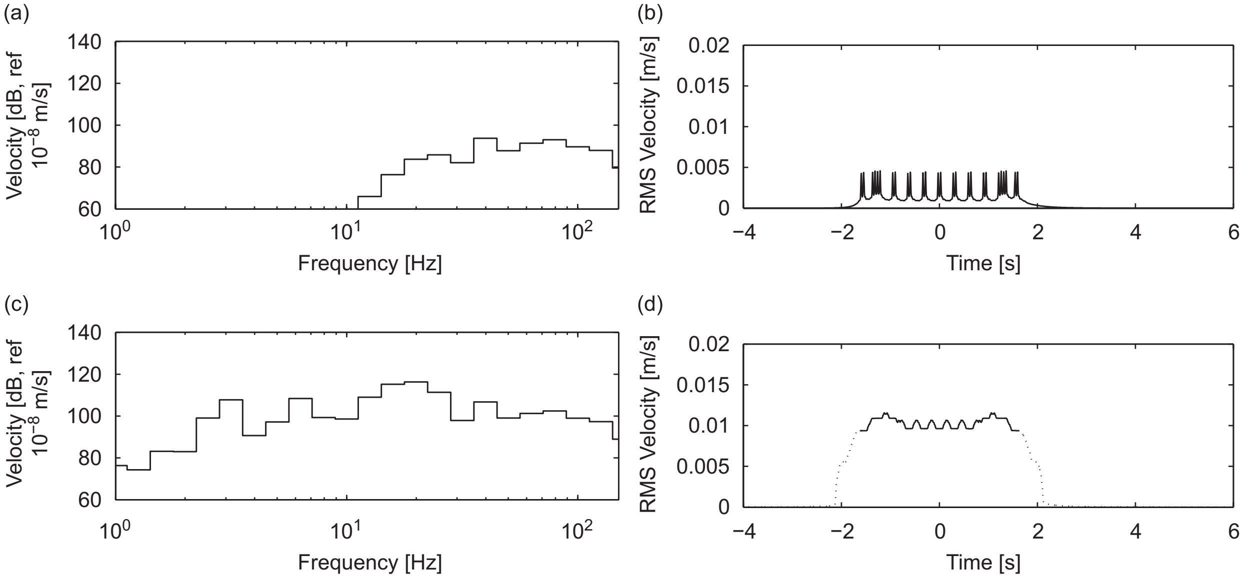

Fig. 20. Vertical sleeper velocity due to a passage of the Thalys HST at a speed v of 218 km/h. Ensemble average of the (a) one-third octave band representation and (b) instantaneous rms value due to dynamic excitation and (c) one-third octave band spectrum and (d) running rms value of the total response. The dotted and solid line in (d) show the running rms value outside and during the DIN 45672-2 reference period T_2, respectively.

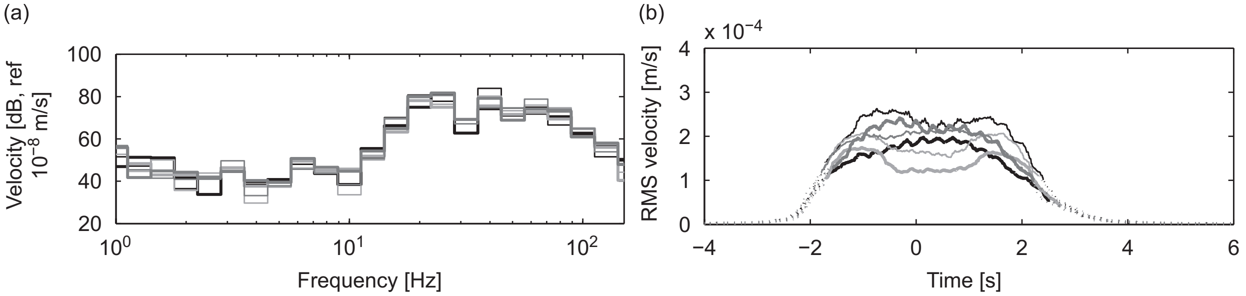

Fig. 21. (a) One-third octave band spectra and (b) running rms value of the free-field velocity at 16 m from the track for 6 samples of vertical track unevenness. The dotted and solid line in (b) show the running rms value outside and during the DIN 45672-2 reference period T_2, respectively.

increases from 156 to 224 km/h. Since the PSD of the unevenness is assumed to be proportional to $k_y^{-3.5}$, the modulus of the perceived unevenness is expected to increase with increasing train speed as $v^{1.25}$. For the given train speeds, this is an increase by 3.9 dB, as observed in Fig. 23a. In Fig. 23b, the train speed increases from 218 to 307 km/h, which results in an increase of the perceived unevenness by 3.7 dB.

Fig. 24 compares one-third octave band spectra of the dynamic load of the first locomotive axle for the InterCity train and the Thalys HST. The narrow-band representation of these spectra has been previously shown in Fig. 7. The predicted dynamic axle load depends on the train speed in two ways, as both the perceived unevenness and the track compliance are affected. For both train types, the dynamic axle load increases with the train speed in a similar way as the perceived unevenness in Fig. 23.

Fig. 25 compares measured and predicted one-third octave band spectra of the sleeper velocity for different train speeds. Fig. 25a and b compare predictions for the passages of the InterCity train and the Thalys HST, respectively, for a single sample of track unevenness. The narrow-band representation of these spectra has

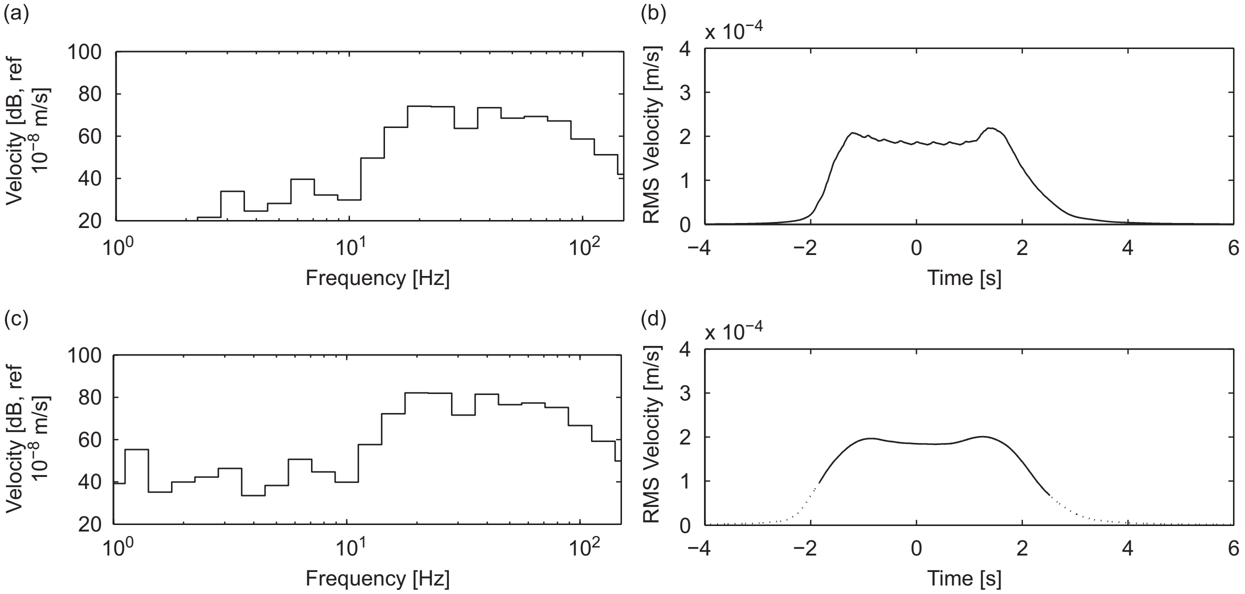

Fig. 22. Vertical free-field velocity at 16 m from the track due to a passage of the Thalys HST at a speed v of 218 km/h. Ensemble average of the (a) one-third octave band representation and (b) instantaneous rms value due to dynamic excitation and (c) one-third octave band spectrum and (d) running rms value of the total response. The dotted and solid line in (d) show the running rms value outside and during the DIN 45672-2 reference period T_2, respectively.

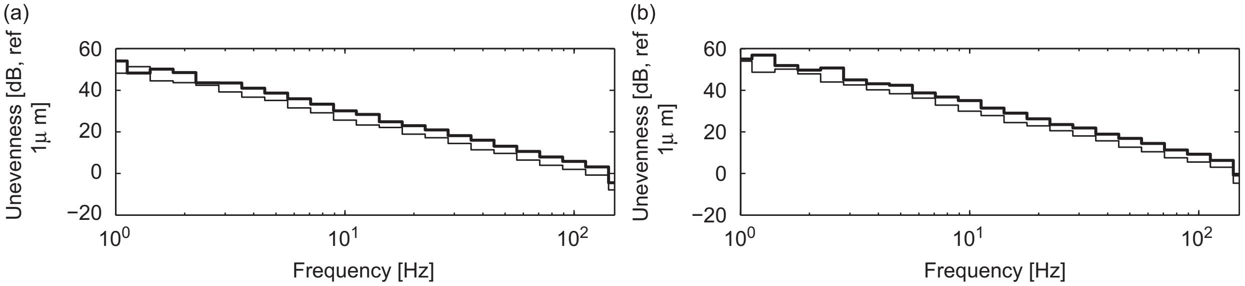

Fig. 23. One-third octave band spectra of the vertical track unevenness for (a) an InterCity train at 156 km/h (thin black line) and 224 km/h (thick black line) and (b) a Thalys HST at 218 km/h (thin black line) and 307 km/h (thick black line).

been previously shown in Fig. 15. As the sleeper velocity is predominantly due to quasi-static excitation, the increase of the dynamic load in Fig. 24 is of little importance. Instead, the one-third octave band spectra show the previously discussed shift to higher frequencies for increasing train speeds (Fig. 15). Due to the dominant quasi-static contribution to the sleeper velocity, the ensemble average response (Figs. 25c and d) is very similar to the response for a single sample. The predictions for a single sample of unevenness and the ensemble average are now compared with the measurements in Figs. 25e and f. The measured response in the frequency bands below 3 Hz is affected by a high-pass filter that has been used to eliminate the DC component and avoid drifting by the integration of the accelerometer data. At higher frequencies above 40 Hz, the sleeper velocity is underestimated. In this frequency range, the sleeper velocity is predominantly due to dynamic excitation (Fig. 13), which seems to be underestimated. The quasi-static contribution to the sleeper velocity at lower frequencies is more accurately predicted, which is due to the successful identification of the dynamic track properties by means of a rail receptance test [16]. Generally, however, a reasonable agreement is obtained, with similar trends for increasing train speeds.

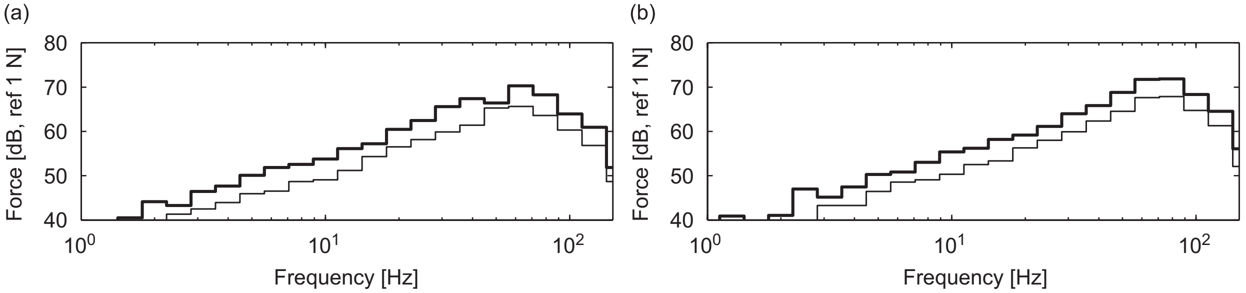

Fig. 24. One-third octave band spectra of the dynamic load of the first locomotive axle for (a) an InterCity train at 156 km/h (thin black line) and 224 km/h (thick black line) and (b) a Thalys HST at 218 km/h (thin black line) and 307 km/h (thick black line).

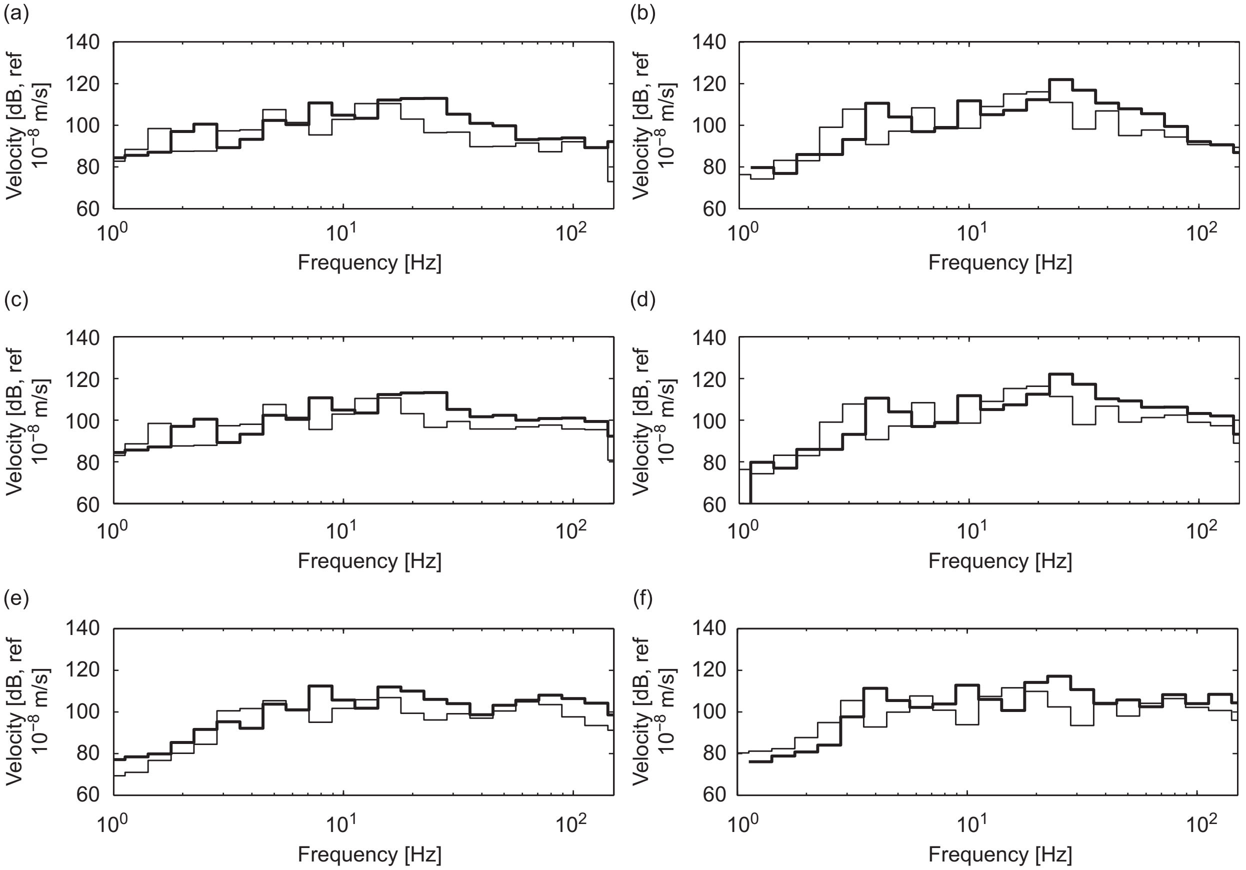

Fig. 25. One-third octave band spectra of the sleeper velocity: (a) a single sample, (c) the ensemble average and (e) measurements for a passage of the InterCity train at 156 km/h (thin black line) and 224 km/h (thick black line) and (b) a single sample, (d) the ensemble average and (f) measurements for a passage of the Thalys HST at 218 km/h (thin black line) and 307 km/h (thick black line).

Fig. 26 compares the measured and predicted running rms value of the sleeper velocity for different train speeds. The predictions for a single sample of track unevenness (Figs. 26a and c) and the ensemble average (Figs. 26c and d) show a clear increase with the train speed. Figs. 26e and f show the corresponding results from field measurements. In the measured rms value for the InterCity train, the distinction between the passage of the axles of the locomotive and the other coaches is less pronounced than in the predictions. Generally, however, similar trends are observed, with increasing vibration levels for higher train speeds and a good quantitative agreement between results from measurements and numerical predictions.

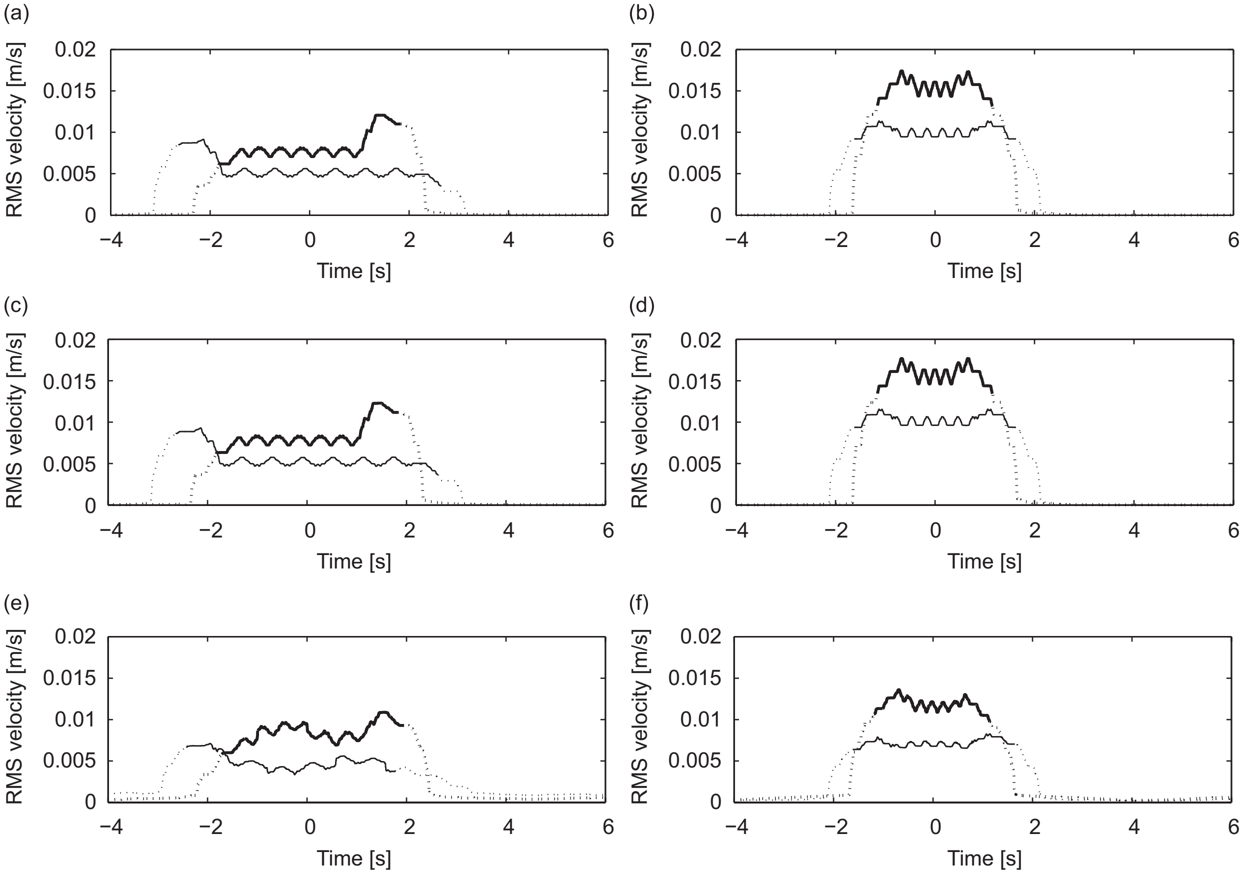

Fig. 26. Running rms value of the sleeper velocity: (a) a single sample, (c) the ensemble average and (e) measurements for a passage of the InterCity train at 156 km/h (thin black line) and 224 km/h (thick black line) and (b) a single sample, (d) the ensemble average and (f) measurements for a passage of the Thalys HST at 218 km/h (thin black line) and 307 km/h (thick black line). The dotted and solid line in (d) show the running rms value outside and during the DIN 45672-2 reference period T_2, respectively.

Fig. 27 compares measured and predicted one-third octave band spectra of the free-field velocity at 16 m from the track for different train speeds. Although the dynamic axle loads increase in the entire frequency range (Fig. 24), a similar trend is not observed in the one-third octave band spectra of the free-field velocity for the single sample of track unevenness (Figs. 27a and b) and the ensemble average (Figs. 27c and d). Similar conclusions hold for the measurements in Figs. 27c and d. Generally, a reasonable agreement is obtained between the results from measurements and numerical predictions. This is due to the successful identification of the dynamic soil properties, based on results from SASW tests, SCPT and transfer functions between the track and the free field [16].

Fig. 28 compares the measured and predicted running rms value of the free-field velocity at 16 m from the track for different train speeds. The results for a single sample of track unevenness (Figs. 28a and b) show a moderate increase of the rms value with the train speed. The ensemble average (Figs. 28c and d), however, shows a clear increase proportional to $v^{1.25}$, as predicted for the dynamic axle loads. These results suggest that, although on average an increase of the train speed is expected, the trend may not be observed for individual samples of track unevenness. Figs. 28e and f show the corresponding results from field measurements. As for the sleeper, the distinction between the passage of the axles of the locomotive and the other carriages is less clear in the measurements than in the predictions. In the case of the Thalys HST, a slight increase of vibration levels with increasing train speed is observed in the measurements.

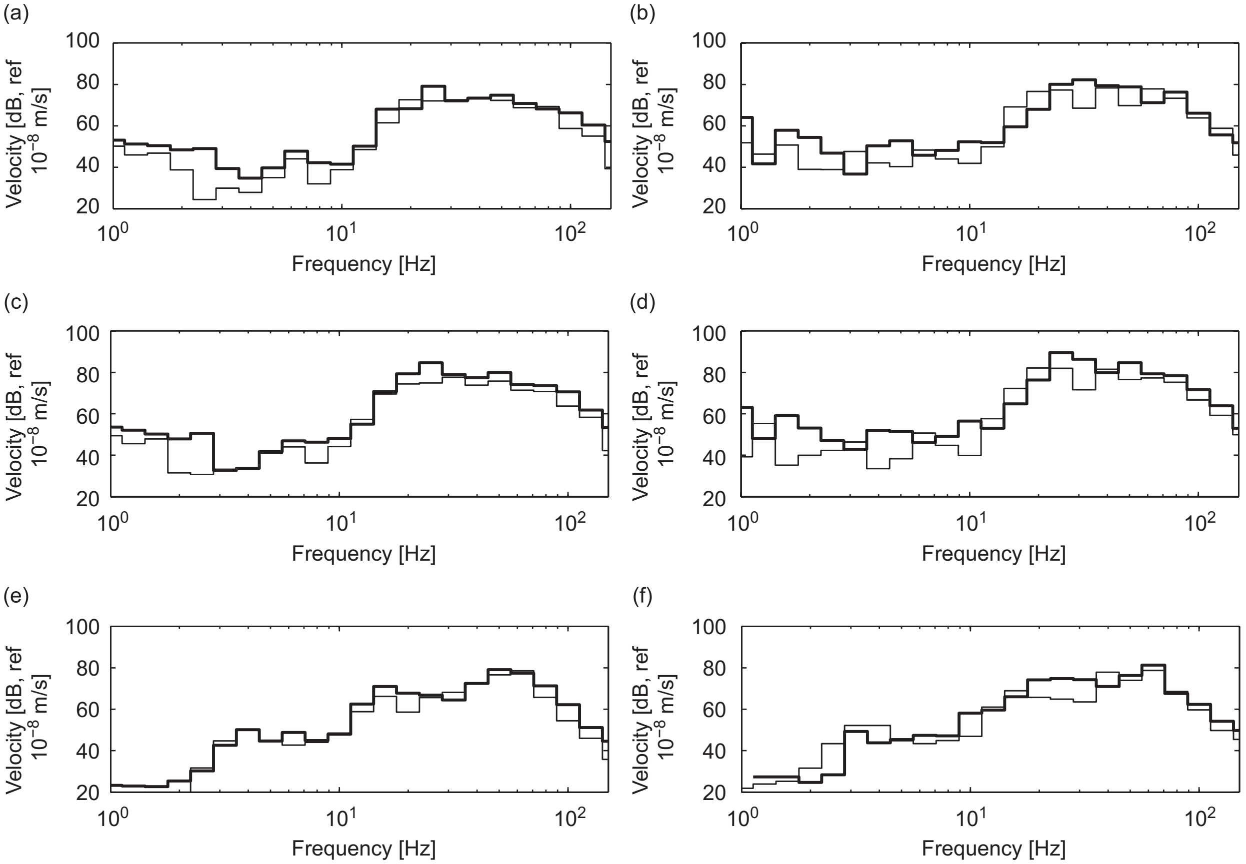

Fig. 27. One-third octave band spectra of the free-field velocity at 16 m from the track: (a) a single sample, (c) the ensemble average and (e) measurements for a passage of the InterCity train at 156 km/h (thin black line) and 224 km/h (thick black line) and (b) a single sample, (d) the ensemble average and (f) measurements for a passage of the Thalys HST at 218 km/h (thin black line) and 307 km/h (thick black line).

4.2. Peak rms value of the vibration velocity for all train passages

In this subsection, a comparison is made of the predicted and measured peak rms value of the velocity for all passages of the InterCity train and Thalys HST during the homologation tests. Fig. 29 shows the peak value of the rms value of the predicted ensemble average and the measured velocity as a function of the train speed. Apart from the response of the sleeper and in the free field at 16 m from the track, the results in the free field at 8, 32, 48 and 64 m from the track are also shown.

The predictions for both train types show a similar trend, with vibration levels that gradually increase with increasing train speed. In the free field, where the dynamic excitation dominates the response, the vibration levels increase by 8 dB when the train speed is raised from 156 upto 330 km/h. The influence of the train speed is therefore similar as for the perceived unevenness, with an increase according to $v^{1.25}$, based on the assumed PSD function of the track unevenness. When the vibration levels at different distances from the track are compared, a decrease of 5–15 dB is found when the distance is doubled.

A comparison of the predicted and measured values shows a very good agreement at small and large distances from the track. At intermediate distances of 32 and 48 m from the track, the agreement is less good, although the difference is not larger than 10 dB. The good agreement at 64 m from the track is partly due to the fact that the transfer function at this distance from the track has been used to estimate the material damping ratio of the soil in the numerical model [16].

In the measurements, the difference between the results for the InterCity train and the Thalys HST is more pronounced, with relatively higher vibration levels for the InterCity train. For each type of train and for most

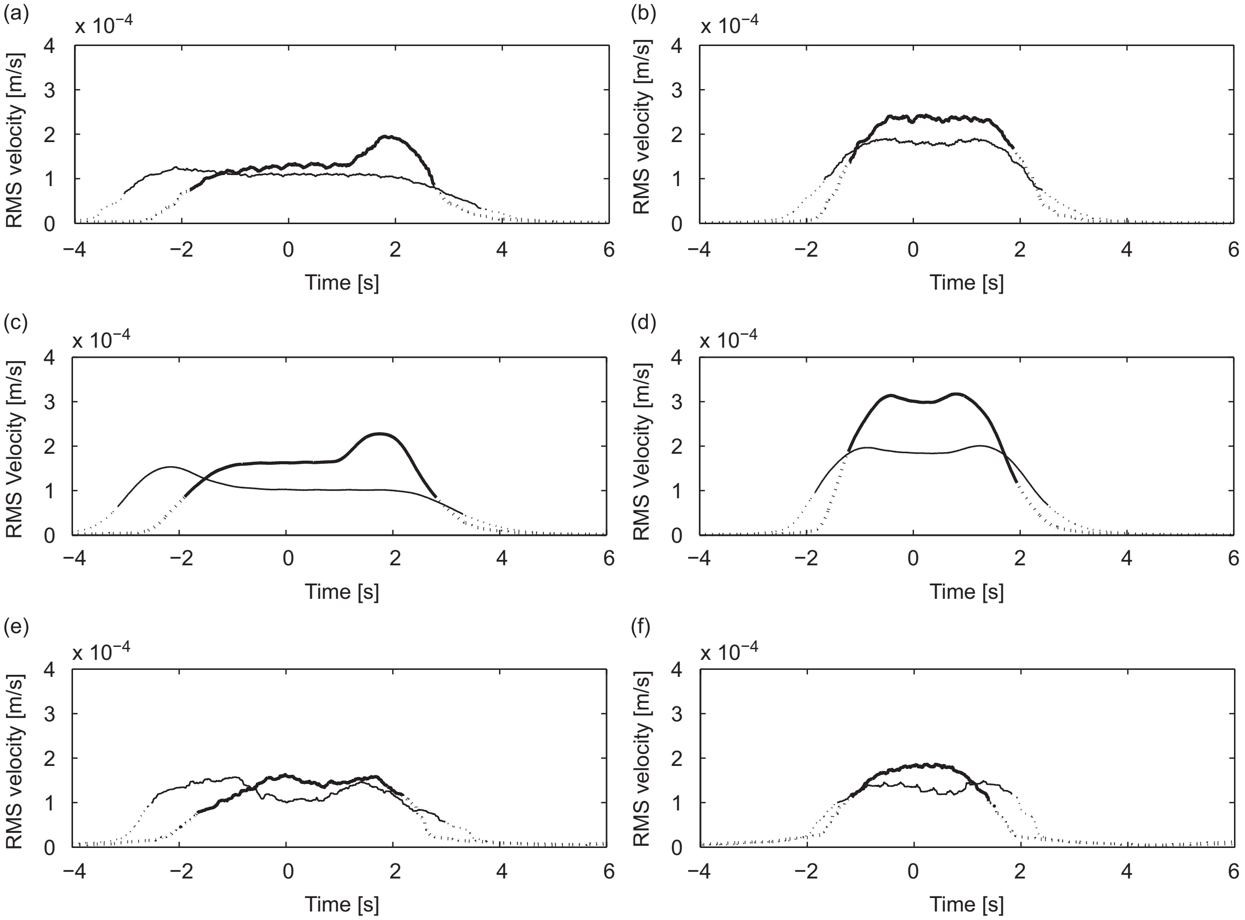

Fig. 28. Running rms value of the free-field velocity at 16 m from the track: (a) a single sample, (c) the ensemble average and (e) measurements for a passage of the InterCity train at 156 km/h (thin black line) and 224 km/h (thick black line) and (b) a single sample, (d) the ensemble average and (f) measurements for a passage of the Thalys HST at 218 km/h (thin black line) and 307 km/h (thick black line). The dotted and solid line in (d) show the running rms value outside and during the DIN 45672-2 reference period T_2, respectively.

points in the free field, a moderate increase of the vibration levels is observed with increasing train speeds. In the case of the InterCity train, the measured vibration levels at 8 m from the track suggest a decrease of vibration levels with the train speed, but this could be due to a single inaccurate result for a speed of 156 km/h. The differences between measurements and predictions may be due to the fact that only a single sample of track unevenness is considered in the experiments or due to an inaccurate model of the track unevenness. If the track unevenness can be represented by the PSD function in Eq. (33), a smaller value of n results in a smaller increase of vibration levels with the train speed and could explain the trend in the measured vibration levels.

5. Conclusion

In this paper, a numerical model for the prediction of railway-induced vibrations is used to evaluate the quasi-static excitation and the dynamic excitation due to random track unevenness. A solution strategy is presented that allows for the evaluation of the non-stationary statistics of the response with a moderate computational cost. The quasi-static and dynamic contribution to the track and free-field response are evaluated for InterCity trains and the Thalys HST. The train speed is in the subcritical range, below the critical phase velocity of the coupled track–soil system. Finally, numerical predictions and field measurements for different train speeds are compared.

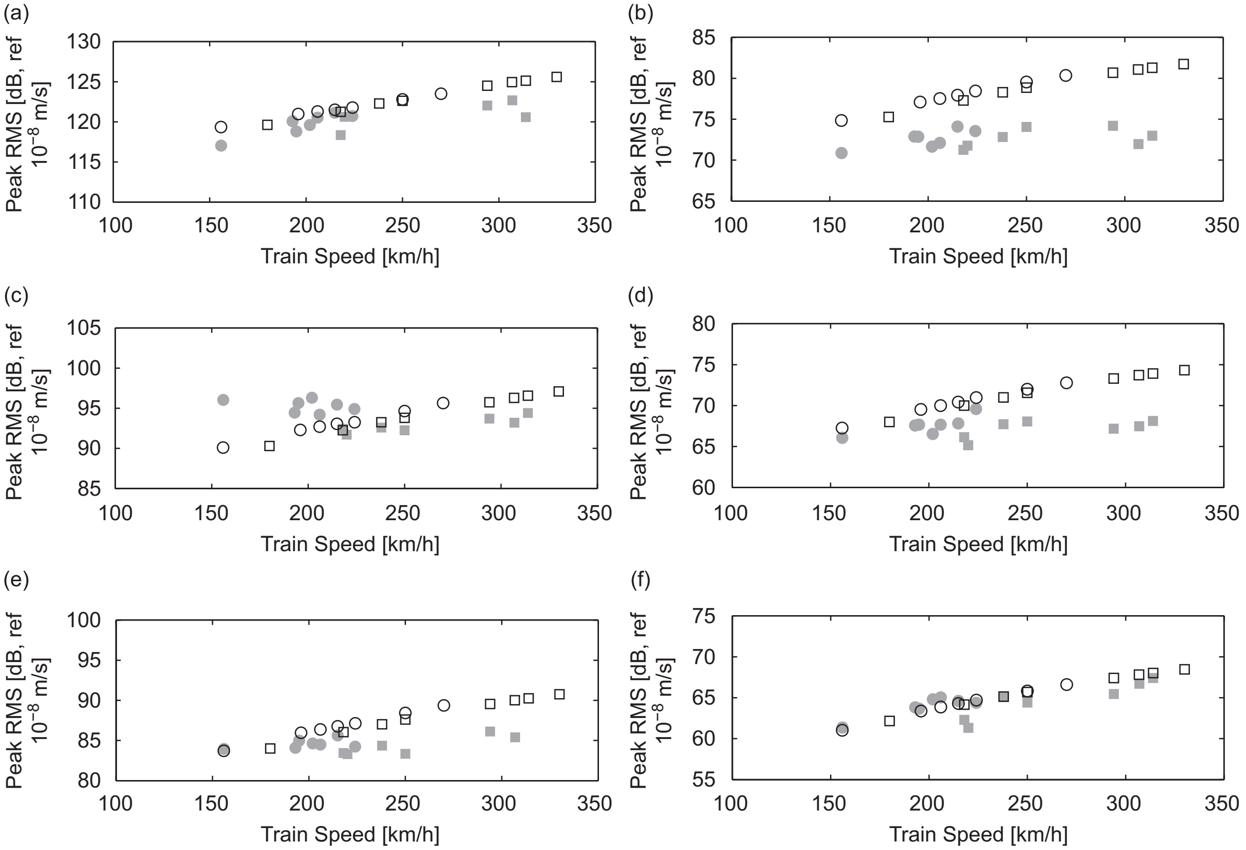

Fig. 29. Predicted ensemble average (black) and measured (grey) peak rms value of the velocity as a function of the train speed for the InterCity train (circles) and the Thalys HST (squares): (a) of the sleeper and in the free field at (b) 8 m, (c) 16 m, (d) 32 m, (e) 48 m and (f) 64 m from the track.

The following conclusions are made for vibrations induced by InterCity and HSTs in the subcritical speed range:

1. The quasi-static contribution dominates the track response, while the free-field response is dominated by the dynamic contribution.
2. Numerical models such as Krylov's model that only account for quasi-static excitation are only well suited to predict the response in the immediate vicinity of the track.
3. The quasi-static track response increases moderately with the train speed.
4. When the dynamic excitation is due to random track unevenness, the influence of the train speed on the free-field vibrations depends on the PSD of the track unevenness.
5. In the case where the PSD function of the unevenness is proportional to k_y^{-n}, the perceived unevenness and the modulus of the dynamic axle loads increase as $v^{(0.5n-1)}$ when $n > 1$.
6. When different samples of the track unevenness are considered, the average free-field response is expected to increase in a similar way with increasing train speed. This trend may not be observed, however, for individual samples of the track unevenness.
7. For a single sample of random track unevenness, the response along the track is a random process as well. If the track unevenness is ergodic, the average response along the track is equal to the ensemble average response.
8. Both measured and predicted free-field vibrations show a very moderate increase with increasing train speed.

(9) Based on a successful identification of the dynamic track and soil characteristics, the peak rms value of the velocity during the passage of InterCity trains and the Thalys HST is predicted with a difference of less than 5 dB for most train speeds and measurement points.

Acknowledgements

The corresponding author is currently holder of a Postdoctoral Fellowship of the Research Foundation—Flanders (FWO—Vlaanderen).

The field measurements presented in this paper have been obtained within the frame of the STWW Project IWT 000152 "Traffic induced vibrations in buildings". These data will be made available to other researchers upon request to the corresponding author.

The financial support of FWO—Vlaanderen and IWT is kindly acknowledged.

References

[1] K. Adolfsson, B. Andréasson, P.-E. Bengtson, A. Bodare, C. Madshus, R. Massarch, G. Wallmark, P. Zackrisson, High speed lines on soft ground. Evaluation and analyses of measurements from the West Coast Line, Technical Report, Banverket, Sweden, 1999.

[2] A.V. Metrikine, S.N. Verichev, J. Blauwendraad, Stability of a two-mass oscillator moving on a beam supported by a visco-elastic half-space, *International Journal of Solids and Structures* 42 (2005) 1187–1207.

[3] K. Knothe, S.L. Grassie, Modelling of railway track and vehicle/track interaction at high frequencies, *Vehicle Systems Dynamics* 22 (1993) 209–262.

[4] M. Heckl, G. Hauck, R. Wettschureck, Structure-borne sound and vibration from rail traffic, *Journal of Sound and Vibration* 193 (1) (1996) 175–184.

[5] J.C.O. Nielsen, A. Igeland, Vertical dynamic interaction between train and track-influence of wheel and rail imperfections, *Journal of Sound and Vibration* 187 (5) (1995) 825–839.

[6] ORE. Question C116: Wechselwirkung zwischen Fahrzeugen und gleis, Bericht No. 1: Spektrale Dichte der Unregelmässigkeiten in der Gleislage. Question C116: Interaction between railway vehicles and track, Report No. 1: Spectral density of track irregularities, Technical Report, Office for Research and Experiments of the International Union of Railways, Utrecht, NL, 1971.

[7] T. Ekevid, N.-E. Wiberg, Wave propagation related to high-speed train. A scaled boundary FE-approach for unbounded domains, *Computer Methods in Applied Mechanics and Engineering* 191 (2002) 3947–3964.

[8] D. Aubry, D. Clouteau, G. Bonnet, Modelling of wave propagation due to fixed or mobile dynamic sources, in: N. Chouw, G. Schmid (Eds.), *Workshop Wave '94, Wave Propagation and Reduction of Vibrations*, Ruhr Universität Bochum, Germany, 1994, pp. 109–121.

[9] X. Sheng, C.J.C. Jones, M. Petyt, Ground vibration generated by a harmonic load acting on a railway track, *Journal of Sound and Vibration* 225 (1) (1999) 3–28.

[10] X. Sheng, C.J.C. Jones, M. Petyt, Ground vibration generated by a load moving along a railway track, *Journal of Sound and Vibration* 228 (1) (1999) 129–156.

[11] X. Sheng, C.J.C. Jones, D.J. Thompson, A comparison of a theoretical model for quasi-statically and dynamically induced environmental vibration from trains with measurements, *Journal of Sound and Vibration* 267 (3) (2003) 621–635.

[12] X. Sheng, C.J.C. Jones, D.J. Thompson, A theoretical model for ground vibration from trains generated by vertical track irregularities, *Journal of Sound and Vibration* 272 (3–5) (2004) 937–965.

[13] A.V. Metrikine, K. Popp, Instability of vibrations of an oscillator moving along a beam on an elastic half-space, *European Journal of Mechanics, A/Solids* 18 (2) (1999) 331–349.

[14] H.A. Dieterman, A.V. Metrikine, The equivalent stiffness of a halfspace interacting with a beam. Critical velocities of a moving load along the beam, *European Journal of Mechanics, A/Solids* 15 (1) (1996) 67–90.

[15] G. Lombaert, G. Degrande, D. Clouteau, Numerical modelling of free field traffic induced vibrations, *Soil Dynamics and Earthquake Engineering* 19 (7) (2000) 473–488.

[16] G. Lombaert, G. Degrande, J. Kogut, S. François, The experimental validation of a numerical model for the prediction of railway induced vibrations, *Journal of Sound and Vibration* 297 (3–5) (2006) 512–535.

[17] G. Lombaert, G. Degrande, B. Vanhauwere, B. Vandeborght, S. François, The control of ground borne vibrations from railway traffic by means of continuous floating slabs, *Journal of Sound and Vibration* 297 (3–5) (2006) 946–961.

[18] J.A. Forrest, H.E.M. Hunt, A three-dimensional tunnel model for calculation of train-induced ground vibration, *Journal of Sound and Vibration* 294 (2006) 678–705.

[19] J.A. Forrest, H.E.M. Hunt, Ground vibration generated by trains in underground tunnels, *Journal of Sound and Vibration* 294 (2006) 706–736.

[20] M.F.M. Hussein, H.E.M. Hunt, A numerical model for calculating vibration from a railway tunnel embedded in a full-space, *Journal of Sound and Vibration* 305 (2007) 401–431.

[21] M.F.M. Hussein, L. Rikse, S. Gupta, H.E.M. Hunt, G. Degrande, J.P. Talbot, S. François, M. Schevenels, Using the PiP model for fast calculation of vibration from a railway tunnel in a multi-layered half-space, *Ninth International Workshop on Railway Noise*, Munich, Germany, September 2007.

[22] X. Sheng, C.J.C. Jones, D.J. Thompson, Prediction of ground vibration from trains using the wavenumber finite and boundary element methods, *Journal of Sound and Vibration* 293 (2006) 575–586.

[23] L. Andersen, C.J.C. Jones, Coupled boundary and finite element analysis of vibration from railway tunnels—a comparison of two- and three-dimensional models, *Journal of Sound and Vibration* 293 (2006) 611–625.

[24] D. Clouteau, M. Arnst, T.M. Al-Hussaini, G. Degrande, Freefield vibrations due to dynamic loading on a tunnel embedded in a stratified medium, *Journal of Sound and Vibration* 283 (1–2) (2005) 173–199.

[25] G. Degrande, D. Clouteau, R. Othman, M. Arnst, H. Chebli, R. Klein, P. Chatterjee, B. Janssens, A numerical model for ground-borne vibrations from underground railway traffic based on a periodic finite element—boundary element formulation, *Journal of Sound and Vibration* 293 (3–5) (2006) 645–666 *Proceedings of the Eighth International Workshop on Railway Noise*, Buxton, UK, 8–11 September 2004.

[26] H. Chebli, R. Othman, D. Clouteau, Response of periodic structures due to moving loads, *Comptes Rendus Mécanique* 334 (2006) 347–352.

[27] S. Gupta, W. Liu, G. Degrande, G. Lombaert, W. Liu, Prediction of vibrations induced by underground railway traffic in Beijing, *Journal of Sound and Vibration* 310 (2008) 608–630.

[28] G. Degrande, L. Schillemans, Free field vibrations during the passage of a Thalys HST at variable speed, *Journal of Sound and Vibration* 247 (1) (2001) 131–144.

[29] G. Degrande, G. Lombaert, An efficient formulation of Krylov's prediction model for train induced vibrations based on the dynamic reciprocity theorem, *Journal of the Acoustical Society of America* 110 (3) (2001) 1379–1390.

[30] R. Paolucci, D. Spinelli, Ground motion induced by train passage, *Journal of Engineering Mechanics, Proceedings of the ASCE* 132 (2) (2006) 201–210.

[31] P. Galvín, J. Domínguez, High-speed train-induced ground motion and interaction with structures, *Journal of Sound and Vibration* 307 (2007) 755–777.

[32] G. Müller, H. Huber, Dynamische Bodeansprachungen infolgte bewegter Lasten, *Bauingenieur* 66 (1991) 375–380.

[33] M. Lieb, Adaptive numerische Fouriertransformation in der Bodendynamik unter Verwendung einer Waveletzerlegung, PhD Thesis, Technische Universität München, München, Germany, 1996.

[34] H. Grundmann, M. Lieb, E. Trommer, The response of a layered half-space to traffic loads moving along its surface, *Archive of Applied Mechanics* 69 (1999) 55–67.

[35] A. Ditzel, G.C. Herman, G.G. Drijkoningen, Seismograms of moving trains: a comparison of theory and measurements, *Journal of Sound and Vibration* 248 (4) (2001) 635–652.

[36] D. Clouteau, G. Degrande, G. Lombaert, Numerical modelling of traffic induced vibrations, *Meccanica* 36 (4) (2001) 401–420.

[37] L. Auersch, The excitation of ground vibration by rail traffic: theory of vehicle–track–soil interaction and measurements on high-speed lines, *Journal of Sound and Vibration* 284 (1–2) (2005) 103–132.

[38] L. Auersch, Ground vibration due to railway traffic—the calculation of the effects of moving static loads and their experimental verification, *Journal of Sound and Vibration* 293 (2006) 599–610.

[39] H. Grundmann, S. Lenz, Nonlinear interaction between a moving SDOF system and a Timoshenko beam/halfspace support, *Archive of Applied Mechanics* 72 (2003) 830–842.

[40] M. Shinozuka, C. Jan, Digital simulation of random processes and its application, *Journal of Sound and Vibration* 25 (1) (1972) 111–128.

[41] M. Shinozuka, G. Deodatis, Simulation of stochastic processes by spectral representation, *Applied Mechanics Reviews* 44 (4) (1991) 191–204.

[42] D.E. Newland, *An Introduction to Random Vibrations, Spectral & Wavelet Analysis*, Longman Scientific & Technical, Essex, England, 1994.

[43] L. Sun, B.S. Greenberg, Dynamic response of linear systems to moving stochastic sources, *Journal of Sound and Vibration* 229 (4) (2000) 957–972.

[44] H. Hao, T.C. Ang, Analytical modelling of traffic-induced ground vibrations, *Journal of the Engineering Mechanics Division, Proceedings of the ASCE* 124 (8) (1998) 921–928.

[45] H.E.M. Hunt, Stochastic modelling of traffic-induced ground vibration, *Journal of Sound and Vibration* 144 (1) (1991) 53–70.

[46] G. Lombaert, G. Degrande, D. Clouteau, The non-stationary free field response for a random moving load, *Journal of Sound and Vibration* 278 (2004) 611–635.

[47] F. Lu, Q. Gaoa, J.H. Lin, F.W. Williams, Non-stationary random ground vibration due to loads moving along a railway track, *Journal of Sound and Vibration* 298 (2006) 30–42.

[48] H.E.M. Hunt, Modelling of road vehicles for calculation of traffic-induced ground vibrations, *Journal of Sound and Vibration* 144 (1) (1991) 41–51.

[49] J. Kogut, G. Degrande, Free field vibrations due to the passage of an IC train and a Thalys high speed train on the L2 track Brussels-Köln, Report BWM-2002-10, Department of Civil Engineering, K.U. Leuven, November 2002, STWW Programme Technology and Economy, Project IWT-000152.

[50] J. Kogut, G. Degrande, Assessment of the dynamic parameters of the HST track L2 Brussels—Köln in Lincent using rail receptance measurements, Report BWM-2003-05, Department of Civil Engineering, K.U. Leuven, March 2003. STWW Programme Technology and Economy, Project IWT-000152.

[51] L. Pyl, G. Degrande, Determination of the dynamic soil characteristics with the SASW method at a site in Lincent, Report BWM-2001-02, Department of Civil Engineering, K.U.Leuven, August 2001, STWW Programme Technology and Economy, Project IWT-000152.
[52] W. Haegeman, In situ tests Retie–Waremme–Lincent, Report RUG IV.1.16.3, Soil Mechanics Laboratory, Ghent University, September 2001, STWW Programme Technology and Economy, Project IWT-000152.
[53] J. Kogut, G. Degrande, Transfer functions between the HST track and the free field on the line L2 Brussels-Köln in Lincent, Report BWM-2003-03, Department of Civil Engineering, K.U. Leuven, January 2003, STWW Programme Technology and Economy, Project IWT-000152.
[54] R. Van Leeuwen, Meetautorail EM130 Documentatie, Technical Report, NMBS, 2002.
[55] H. Braun, T. Hellenbroich, Messergebnisse von Strassenunebenheiten, *VDI Berichte* 877 (1991) 47–80.
[56] Deutsches Institut für Normung, *DIN 45672 Teil 2*: *Schwingungsmessungen in der Umgebung von Schienenverkehrswegen*: *Auswerteverfahren*, 1995.
[57] V.V. Krylov, On the theory of railway-induced ground vibrations, *Journal de Physique IV* 4 (C5) (1994) 769–772.
[58] V.V. Krylov, Generation of ground vibrations by superfast trains, *Applied Acoustics* 44 (1995) 149–164.
[59] H. Takemiya, Simulation of track–ground vibrations due to a high-speed train: the case of X-2000 at Ledsgard, *Journal of Sound and Vibration* 261 (2003) 503–526.
[60] P. Galvín, J. Domínguez, Analysis of ground motion due to moving surface loads induced by high-speed trains, *Engineering Analysis with Boundary Elements* 31 (2007) 931–941.
[61] International Organization for Standardization. ISO 2631-2:1999: Mechanical vibration and shock—evaluation of human exposure to whole-body vibration—part 2: vibration in buildings (1 to 80 Hz), 1999.